Multiphase-field modelling of anisotropic elasticity at finite deformation in Eulerian space

Simon Daubner[a,c], Martin Reder[a,b,c], Nishant Prajapati[a,c], Daniel Schneider[a,b], Britta Nestler[a,b]

[a] *Institute for Applied Materials (IAM-MMS), Karlsruhe Institute of Technology, Strasse am Forum 7, 76131, Karlsruhe, Germany*
[b] *Institute of Digital Materials Science (IDM), Karlsruhe University of Applied Sciences, Moltkestrasse 30, 76133 Karlsruhe, Germany*
[c] *These authors contributed equally to this work.*

Abstract

This paper presents a novel computational framework for simulating finite deformation elasticity in Eulerian space combined with the multi-phase field method. A key novel aspect of this work is the phase-field mapping method developed to track interfaces (e.g. grain boundaries) in a multi-phase system (e.g. electrode microstructure) undergoing large deformation. The elastic material response is modelled employing a polyconvex, cubic anisotropic material law which has been implemented in the multiphase-field context and validated using benchmark cases. The performance of this framework is demonstrated through representative numerical examples. The model is well-suited for the simulation of multi-crystalline samples where different phases may possess distinct elastic properties and anisotropies which is shown exemplarily for the electrode calendering process at the nano-scale. Additionally, Kelvin-Voigt visco-elasticity is included in the model which allows for simulation of large deformation in an aerogel under compressive load and, furthermore, enables treatment of fluid structure interaction within a common configuration. Finally, a broad outlook of technical applications as well as model extensions is given.

Keywords: finite deformation elasticity, multiphase-field method, reference map, fluid structure interaction

1. Introduction

Microstructural processes which are driven by large elastic and plastic deformations can be found in various fields of engineering, be it biomechanics or battery technologies, among others. In the field of biomechanics, certain biological cells (e.g. blood cells) undergo deformations in the finite strain regime and exhibit a highly non-linear viscoelastic material behaviour [1]. The elastic properties of these cells serve as an indicator of their state, thereby facilitating the diagnosis of diseases [2, 3]. In the field of battery technologies, large mechanical deformations can occur during fabrication as well as during cycling. During battery cycling, some electrode materials undergo large elastic deformations which can lead to fracture or other phase transformation phenomena. The difference in volume between the fully charged and discharged states is about 17% in $NaFePO_4$ [4], 80% in the lithium-sulfur conversion reaction [5], and as high as 300% in silicon-based anodes for lithium batteries [6]. Furthermore, battery electrodes exhibit a porous microstructure, which introduces additional challenges for modelling the deformation processes. All the above-mentioned applications are of high technological interest, and thereby demand a better fundamental understanding of the underlying microstructural processes.

Numerical modelling of these processes not only poses the computational challenge associated with large deformations, but also of strongly coupled physical fields and interactions. Battery materials are governed by a rich interplay of electro-chemical and elastic forces [7] and the consistent coupling compliant with thermodynamic principles is a non-trivial task. Over the past years, the *phase-field method* (PFM) has established itself as a powerful tool for investigation of phase transformation processes driven by various physical forces (e.g. capillary, chemical and

Email addresses: simon.daubner@kit.edu (Simon Daubner), martin.reder@kit.edu (Martin Reder), nishant.prajapati@kit.edu (Nishant Prajapati), daniel.schneider@kit.edu (Daniel Schneider), britta.nestler@kit.edu (Britta Nestler)

mechanical) as described in review articles [8–10]. An important feature in this context is its capability to naturally describe the motion of evolving interfaces driven by these forces without having to explicitly track the position of the interface. This is achieved by replacing the sharp interface between neighbouring phases with a smooth diffuse interface region, where physical fields vary continuously and phase-inherent quantities are interpolated. Some prominent applications of this approach include solidification [11], anisotropic crystal growth [12, 13] and dissolution [14], multi-phase flow [15, 16] as well as intercalation in battery materials [6, 17, 18]. In the field of solid mechanics, the PFM is nowadays well-established for the modelling of fracture mechanics, see e.g. [19–21], where a crack phase-field is introduced as a regularization of the corresponding sharp interface problem. This approach naturally describes crack initiation and branching and has been included into classical FEM frameworks such as ABAQUS [22]. The investigation of solid-solid phase transitions as in martensitic steels, on the other hand, has generated a large variety of phase-field models that combine a diffuse parametrization of phase boundaries (e.g. grains) with mechanical driving forces [23, 24]. These models often rely on a multiphase-field description [9, 25, 26] to describe phase transitions within polycrystalline microstructures [27]. Different interpolation methods of stresses in the diffuse interface region have been discussed [28, 29], also in the context of large deformations in a Lagrangian framework [30–32].

Efforts to account for large mechanical deformations within the PFM have been undertaken using different approaches. For instance, the work by Chen *et al.* [6] is based on the *classical Cahn-Hilliard* equation. They utilized the local concentration as an order parameter which is coupled to large elasto-plastic deformations. They pointed out that, in order to determine the local concentration and also distinguish between the crystalline and amorphous states, two fields (i.e. concentration and an order parameter) are necessary. The phase-field variables (also called order parameters) are non-conserved and, thus, their evolution is governed by *Allen-Cahn* equations. Modelling of processes which include more than two phases, like electrode calendering, cycling of polycrystalline materials and fluid interaction with various solid bodies, calls for a consistent description of multiple order parameters. While these multi-physics are the motivation for our work and will be addressed in the future, the present work is mainly focused on large deformation mechanics while the phase variables are employed for parametrization of various physical phases (e.g. grain with varying orientation or different stiffnesses). However, inclusion of phase transformations within this framework is straight-forward.

Generally, finite deformation problems can be solved in two different frames of reference:

1. *Lagrangian description*: This frame of reference is set in the material configuration. Formulations in this material coordinates treat free and moving boundaries in a natural manner. However, it suffers from large numerical errors if the mesh is highly distorted. Typical applications include simulation of large deformations using the finite element method [33].
2. *Eulerian description*: This approach is based on the current configuration and, therefore, is free from mesh distortion. It is commonly used in fluid mechanics and thus in the field of fluid structure interaction (e.g. biological applications [34]), it can be beneficial to also treat the solid in the same configuration and thus have one common mesh [35, 36]. Operation in Eulerian space requires the consideration of convective terms, which poses a numerical challenge in the sense that many discretization schemes feature numerical diffusion and introduce errors to the convective transport of constitutive variables.

In this work, we pursue an approach based on the Eulerian frame of reference for various reasons. Firstly, the multiphase-field framework employed here is based on a equidistant Cartesian grid, where the set of coupled partial differential equations are discretized using finite difference schemes. This procedure easily accounts for representative volume elements (RVEs) which are often encountered in microstructure simulation, and furthermore, allows for massive parallelization using Message passing interface (MPI) [37]. Moreover, as the PFM naturally includes interface tracking in the evolution of order parameters, no additional computationally challenging method is needed. At very large deformations, the Eulerian frame may be more robust than the Lagrangian counterpart, as mesh distortion is omitted [38]. Finally, consideration of fluid structure interaction within a single configuration is enabled, since fluid flow is typically treated in an Eulerian framework. Applicability is shown for elastic bodies immersed in weakly compressible fluid within this work.

Multiphase-field approaches that are based on Allen-Cahn equations and include large deformations in the Eulerian frame can also be found in literature. For instance, Borukhovich *et al.* [38] combined a spectral solver on regular grids to compute multiple small deformation steps with a convection scheme, in order to solve large

deformations in the Eulerian frame of reference. However, this approach is limited to periodic boundaries. Even during pure elastic deformations, the phase-field evolution is utilized as an interface stabilisation mechanism, which counteracts undesirable modelling artefacts like numerical diffusion and interface distortion [39]. These artefacts occur due to numerical errors that are introduced by the discretisation of the convective terms of the balance equations. However, such an approach hinders the correct interface movement and artificially lowers the interface velocity [38].

Another important aspect of modelling large deformations is the correct formulation of a constitutive relation. In the case of rate formulations (hypo-elastic materials) the work-conjugacy of stress and strain measures needs to be fulfilled [40]. The class of hyperelastic (Green elastic) materials on the other hand, is characterized by a potential function that describes the stored free energy during deformation. Polyconvexity of this function is a sufficient criterion for the existence of an equilibrium state for the elastic boundary-value problem [41]. While, some material models like the Moonley-Rivlin and Odgen materials satisfy the criterion of polyconvexity [41], the widely used Sait Venant-Kirchhoff law, which is geometrically non-linear but physically linear, does not [42]. Despite the fact that the non-polyconvexity of the Saint Venant-Kirchoff material law has been shown as early as 1986 [42], many recent works [43, 44] are still based on this constitutive relation due to its straight-forward implementation. It performs decently well in cases of large rigid body motion (translation and rotation) combined with small strains but fails at high strains due to its linearity. Some loads may lead to cases where the invertibility of the deformation gradient is not ensured.

In the present work, we utilize a polyconvex constitutive relation for cubic materials based on the work of Kambouchev et al. [45], and systematically demonstrate the material response of different multiphase materials undergoing extremely large elastic deformations. Furthermore, we introduce a *Phase-field Mapping* approach to circumvent the previously discussed discretization artefacts of the convective term. This allows us to reduce the numerical errors induced by the convective scheme which result in distortion of diffuse interfaces, thereby severely affecting the correct tracking of grain boundaries in deforming microstructures. Details will be presented in the following sections, which are organized as follows: Section 2 discusses the computational method including the model equations for I) kinematics, II) balance equations in the Eulerian space, III) constitutive relation, and IV) the multiphase-field formulation in the context of large deformation. In Sec. 3, the implementation and performance of the modelling framework are validated through representative numerical examples. Section 4 contains application examples namely the battery electrode calendering on nano-scale, an aerogel under compressiv load, and the deformation of a biological cell within a channel flow. Finally, the paper is concluded by recapitulating the important highlights and scientific contributions of the present work, followed by an outlook for further extensions in Sec. 5.

2. Finite deformation elasticity in Eulerian framework

2.1. Kinematics

We consider the motion of a homogeneous body $\mathcal{B}$ in a continuum representation described by a motion function $\boldsymbol{\chi} : (\boldsymbol{X}, t) \mapsto \boldsymbol{x}$. The motion function maps each material point $\boldsymbol{X}$ in the initial configuration $\mathcal{B}_0$ at $t = 0$ to the corresponding spatial point $\boldsymbol{x}$ in the current configuration $\mathcal{B}$ at any time $t > 0$, as depicted in Fig. 1. In the Eulerian frame of reference, all fields are parametrized with respect to spatial points $\boldsymbol{x}$, which correspond to the current position of material points located at $\boldsymbol{X}$ in the initial configuration. The inverse motion function, or so-called *reference map* $\boldsymbol{\xi}(\boldsymbol{x}, t) = \boldsymbol{\chi}^{-1}(\boldsymbol{x}, t)$, maps the current position $\boldsymbol{x}$ (at $t > 0$) of a material point to its initial one $\boldsymbol{X}$, and thus

$$\boldsymbol{X} = \boldsymbol{\xi}\left(\boldsymbol{x}, t\right),$$

as also illustrated in Fig. 1. In the present approach, we choose the inverse motion function $\boldsymbol{\xi}$ and spatial velocity $\boldsymbol{v}$ as the primary variables, similar to the works of Kamrin *et al.* [36, 46]. As the initial position $\boldsymbol{X}$ of all material points is constant with respect to time, an equation for the evolution of the inverse motion is derived by requiring the material time derivative given by $\dot{(\cdot)}$ of the reference map $\boldsymbol{\xi}$ to be zero, thereby resulting in the following initial value problem

$$\dot{\boldsymbol{\xi}} = \frac{\partial \boldsymbol{\xi}}{\partial t} + \boldsymbol{v} \cdot (\nabla \boldsymbol{\xi}) = \boldsymbol{0}, \qquad \boldsymbol{\xi}(\boldsymbol{x}, t = 0) = \boldsymbol{x}, \tag{1}$$

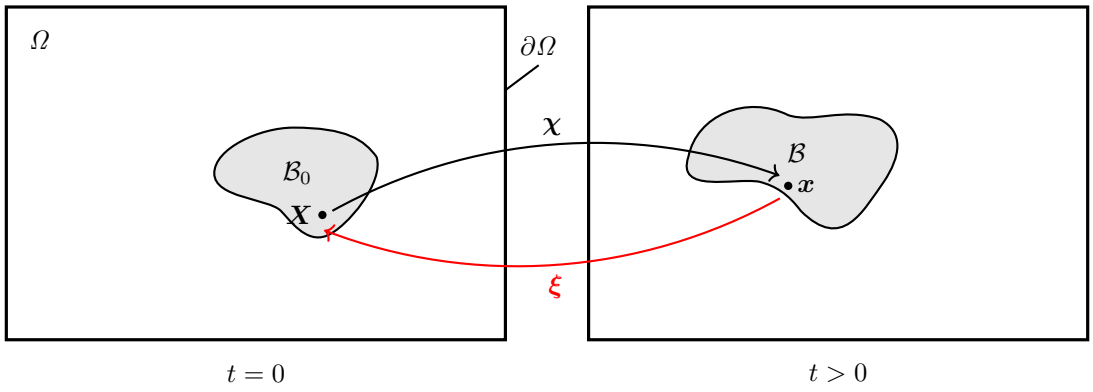

Figure 1: Initial and current configuration of a body $\mathcal{B}$ inside the spatially fixed computational domain Ω and illustration of the inverse motion function $\boldsymbol{\xi}$.

where the ∇ denotes the spatial gradient operator with respect to current position $\boldsymbol{x}$. Eq. (1) represents a convective transport equation for the reference map. In contrast to other widely used tensorial fields such as the deformation gradient [47–49] or the left Cauchy-Green tensor [50] as primary variables, the reference map $\boldsymbol{\xi}$ is a vectorial quantity. The numerical solution of the vectorial convective transport equation is computationally cheaper as compared to the corresponding equations of tensor fields, which are based on the upper-convected Maxwell time derivative. In the latter case, the overhead not only arises from the higher number of components, that need to be considered, but also from an additional term entering the transport equation of tensor fields compared to the one of vector fields [50]. The deformation gradient in spatial parametrization is given in terms of the reference map by

$$\boldsymbol{F}(\boldsymbol{x}, t) = \left(\nabla \boldsymbol{\xi}(\boldsymbol{x}, t)\right)^{-1}. \tag{2}$$

In order to model coupled multiphysics phenomena involving e.g. thermal and diffusion processes, the corresponding contributions to the deformation gradient (i.e. temperature dependent part $\boldsymbol{F}_T\,(T)$, chemical contribution $\boldsymbol{F}_\mathrm{c}(\boldsymbol{c})$ dependent on the concentration tuple $\boldsymbol{c}$ of the species, and so on) are separated by a multiplicative split. Thus, the elastic deformation gradient $\boldsymbol{F}_\mathrm{el}$ can be generally formulated as

$$\boldsymbol{F}_\mathrm{el} = \boldsymbol{F}\boldsymbol{F}_T^{-1}(T)\boldsymbol{F}_\mathrm{c}^{-1}(\boldsymbol{c})\ldots, \tag{3}$$

where the symbol $(\ldots)$ in eq. (3) indicates that further contributions could be accounted for. In the large deformation regime, the absolute deformation measures namely the elastic left and right Cauchy-Green tensors (denoted by $\boldsymbol{B}$ and $\boldsymbol{C}$, respectively) are given by

$$\boldsymbol{B} := \boldsymbol{F}_\mathrm{el}(\boldsymbol{F}_\mathrm{el})^\top \quad \text{and} \quad \boldsymbol{C} := (\boldsymbol{F}_\mathrm{el})^\top \boldsymbol{F}_\mathrm{el}.$$

2.2. Balance equations in the Eulerian space

The mechanics of materials is governed by the mechanical balance equations for mass and momentum. The momentum balance in Eulerian space is given by

$$\rho\dot{\boldsymbol{v}} = \rho\boldsymbol{b} + \nabla\cdot\boldsymbol{\sigma}, \tag{4}$$

where $\rho(\boldsymbol{x}, t)$ denotes the current mass density, $\boldsymbol{\sigma}(\boldsymbol{x}, t)$ represents the Cauchy stress tensor, and $\boldsymbol{b}(\boldsymbol{x}, t)$ is a body force (given per mass in $\mathrm{m\,s^{-2}}$ e.g. gravity). The balance of mass is ensured by requiring the material mass density $\rho^0(\boldsymbol{X})$ to be time invariant in the initial configuration. It is related to the current mass density ρ via

$$\rho^0 = J\rho, \tag{5}$$

where $J := \det(\boldsymbol{F})$ denotes the determinant of the deformation gradient, which represents a local volume change in the current configuration with respect to the initial one. Note, that in the Eulerian framework, the quantities in

eq. (5) are parametrized with respect to $(\boldsymbol{x}, t)$ and thus $\rho^0(\boldsymbol{X}) = \rho^0(\boldsymbol{\xi}(\boldsymbol{x}, t))$ introduces a time dependency. The material time derivative of the velocity $\dot{\boldsymbol{v}}$ in eq. (4) is given by

$$\rho\dot{\boldsymbol{v}} = \rho\left(\frac{\partial \boldsymbol{v}}{\partial t} + \boldsymbol{v}\cdot\nabla\boldsymbol{v}\right) = \frac{\partial}{\partial t}(\rho\boldsymbol{v}) + \nabla\cdot(\rho\boldsymbol{v}\otimes\boldsymbol{v}) \tag{6}$$

where the operator $\otimes$ denotes the dyadic product. The last part in eq. (6) is obtained by utilising the mass balance.

2.3. Constitutive law

In addition to the kinematic relations in Sec. 2.1, constitutive equations relating the stress and deformation are required in order to complete the system of balance equations. The stored elastic free energy of a solid body under mechanical loading should be at minimum in mechanical equilibrium. Consequently, the existence of an equilibrium solution for the elastic boundary value problem (with arbitrary Dirichlet boundary conditions) needs to be ensured by the choice of the respective material law. Therefore, the stored elastic free energy must satisfy the convexity conditions (see Ball [41]). The elastic free energy density takes the form

$$f_{\mathrm{el}}(\boldsymbol{F}_{\mathrm{el}}) = g(\boldsymbol{F}_{\mathrm{el}}, \operatorname{adj}\boldsymbol{F}_{\mathrm{el}}, \det\boldsymbol{F}_{\mathrm{el}}),$$

g being a convex function and adj() denoting the adjugate of a tensor. In the present work, we employ a free energy formulation for materials with cubic symmetry proposed by Kambouchev *et al.* [45], that satisfies convexity. The stored elastic free energy based on the *Kambouchev law* is formulated as a linear combination of polyconvex monomials of the elastic right Cauchy-Green tensor $\boldsymbol{C}$

$$f_{\mathrm{el}}(\boldsymbol{C}) = -k_1\ln(\det(\boldsymbol{C})) + k_2\det(\boldsymbol{C}) + k_3\operatorname{tr}^2(\boldsymbol{M}\boldsymbol{C}) + k_4\operatorname{tr}(\boldsymbol{C}), \tag{7}$$

where $\operatorname{tr}(\cdot)$ denotes the trace of a tensor. The tensorial object $\boldsymbol{M}$ in eq. (7) is a structural tensor representing the material symmetry. For materials exhibiting cubic symmetry, $\boldsymbol{M}$ takes the following form

$$\boldsymbol{M} = \sum_{\iota=1}^{3}\boldsymbol{v}_\iota\otimes\boldsymbol{v}_\iota,$$

where $\boldsymbol{v}_\iota\ \forall\,\iota\in\{1,2,3\}$ denote the three orthogonal privileged directions of the cubic anisotropy. From the coefficients $k_i\ \forall\, i\in\{1,2,4\}$ in eq. (7) only two are independent. They are related to the Lamé constants λ and μ as by

$$k_1 = (\lambda+2\mu)/4, \quad k_2 = \lambda/4, \quad k_4 = \mu/2.$$

The third coefficient k_3 in eq. (7) accounts for the strength of cubic anisotropy in the material law, and serves as the third material stiffness parameter in addition to the two Lamé constants. The anisotropic formulation with $k_3 \neq 0$ is well-suited for simulating the material response of polycrystalline structures, where each crystal exhibits a random crystallographic orientation in space. For the choice $k_3 = 0$, the third term (containing structural tensor $\boldsymbol{M}$) in eq. (7) vanishes, resulting in the isotropic formulation of the constitutive law. From the stored elastic free energy function eq.(7), the second Piola-Kirchoff stress tensor $\boldsymbol{S}$ is computed as

$$\boldsymbol{S} = 2\frac{\partial f_{\mathrm{el}}(\boldsymbol{C})}{\partial\boldsymbol{C}} = 2\Big(-k_1\boldsymbol{C}^{-1} + k_2\det(\boldsymbol{C})\boldsymbol{C}^{-1} + 2k_3\operatorname{tr}(\boldsymbol{M}\boldsymbol{C})\boldsymbol{M} + k_4\boldsymbol{I}\Big), \tag{8}$$

where $\boldsymbol{I}$ denotes the second order identity tensor. In order to use this constitutive law within the Eulerian framework, a formulation with respect to the Cauchy stress tensor $\boldsymbol{\sigma}$ is required. This can be derived from eq. (8) using the transformation $\boldsymbol{\sigma} = (\boldsymbol{F}\boldsymbol{S}\boldsymbol{F}^T)/J$. The transformation can be simplified in the absence of inelastic strains, i.e. $\boldsymbol{F} = \boldsymbol{F}_{\mathrm{el}}$ holds, such that eq. (8) can be re-formulated in terms of the Cauchy stress as

$$\boldsymbol{\sigma} = \frac{2}{J}\Big(k_4\boldsymbol{B} + (k_2J^2 - k_1)\boldsymbol{I} + 2k_3\operatorname{tr}(\boldsymbol{M}\boldsymbol{C})\boldsymbol{F}\boldsymbol{M}\boldsymbol{F}^\top\Big). \tag{9}$$

Using the following relations derived from tensor algebra

$$\boldsymbol{F}\boldsymbol{M}\boldsymbol{F}^{\top} = \sum_{\iota=1}^{3} \boldsymbol{F}\boldsymbol{v}_\iota \otimes \boldsymbol{F}\boldsymbol{v}_\iota \quad \text{and} \quad \operatorname{tr}(\boldsymbol{M}\boldsymbol{C}) = \sum_{\iota=1}^{3} \boldsymbol{v}_\iota \cdot \boldsymbol{C}\boldsymbol{v}_\iota = \sum_{\iota=1}^{3} \boldsymbol{F}\boldsymbol{v}_\iota \cdot \boldsymbol{F}\boldsymbol{v}_\iota,$$

and substituting them into eq. (9), the final expression for the Cauchy stress tensor reads

$$\boldsymbol{\sigma} = \frac{2}{J}\left[k_4\boldsymbol{B} + (k_2 J^2 - k_1)\boldsymbol{I} + 2k_3 \sum_{\iota=1}^{3} (\tilde{\boldsymbol{v}}_\iota \cdot \tilde{\boldsymbol{v}}_\iota)\tilde{\boldsymbol{v}}_\iota \otimes \tilde{\boldsymbol{v}}_\iota\right], \tag{10}$$

where $\tilde{\boldsymbol{v}}_\iota := \boldsymbol{F}\boldsymbol{v}_\iota$ denotes the transformed priviledged direction. Eq. (10) relates the Cauchy stress tensor to the Left Cauchy-green deformation tensor $\boldsymbol{B}$ for materials obeying cubic anisotropy according to the Kambouchev law. The Kambouchev Material law can be generalized for other symmetry groups via a general invariant formulation of the anisotropic constitutive equation cf., e.g., [51]. Let $\{\boldsymbol{v}_1, \boldsymbol{v}_2, \boldsymbol{v}_3\}$ be three orthogonal vectors and

$$\boldsymbol{M}_{\iota\kappa} = \boldsymbol{v}_\iota \otimes \boldsymbol{v}_\kappa, \qquad \iota, \kappa \in \{1, 2, 3\}$$

the corresponding structural tensors, then the anisotropic part of the second Piola-Kirchhoff stress can be expressed via

$$\begin{aligned}
\boldsymbol{S}^{\text{aniso}} &= \sum_{\iota=1}^{3} \alpha_{\iota\iota}\boldsymbol{M}_{\iota\iota} + \sum_{\iota=2}^{3}\sum_{\kappa=1}^{\iota} \alpha_{\iota\kappa}\left(\boldsymbol{M}_{\iota\kappa} + \boldsymbol{M}_{\kappa\iota}\right), \\
\alpha_{\iota\kappa} &= \alpha_{\iota\kappa}\left(\operatorname{tr}(\boldsymbol{M}_{11}\boldsymbol{C}), \ldots, \operatorname{tr}(\boldsymbol{M}_{13}\boldsymbol{C}), \ldots, \operatorname{tr}(\boldsymbol{M}_{33}\boldsymbol{C})\right).
\end{aligned}$$

The special case of cubic anisotropy is retrieved with the choice $\alpha_{11} = \alpha_{22} = \alpha_{33} = 2k_3 \sum_\iota \operatorname{tr}(\boldsymbol{M}_{\iota\iota}\boldsymbol{C})$ and $\forall \iota \neq \kappa : \ \alpha_{\iota\kappa} = 0$. In addition to elasticity, it is straightforward to include Kelvin–Voigt viscoelastic material behaviour in the present model by additionally considering the viscous stress term

$$\boldsymbol{\sigma}^{\text{visc}} = \eta\left(\nabla\boldsymbol{v} + \nabla^{\top}\boldsymbol{v}\right) + \left(\zeta - \frac{2}{3}\eta\right)\nabla \cdot \boldsymbol{v}\,\boldsymbol{I}, \tag{11}$$

where η denotes the dynamic and ζ the volumetric viscosity. The viscous stress term can be directly calculated from the velocity field $\boldsymbol{v}$ obtained from Eq. (6). While the validation cases in Sec. 3 are purely elastic, some application examples include viscous effects.

2.4. Multiphase-field formulation

In order to describe a multigrain system with N solid phases, we consider a tuple $\boldsymbol{\phi} = \{\phi_1, \ldots, \phi_N\}^T$ of N order parameters known as the *phase-fields*. Each phase-field parameter $\phi_\alpha(\boldsymbol{x}, t) \in [0, 1]$ represents the local volume fraction of phase $\alpha \in \{1, \ldots, N\}$ at the spatial position $\boldsymbol{x}$ and time t. The solid phases may differ in elastic and/or structural properties. The interfaces between neighbouring phases (e.g. grain boundaries in a multigrain system, fracture surface in a cracked-specimen) are parametrized by a smooth but steep transition region, the diffuse interface. At any point in time and space, the Gibbs simplex constraint $\mathcal{G} = \left\{\boldsymbol{\phi} \in \mathbb{R}^N : \sum_\alpha \phi_\alpha = 1, \phi_\alpha \geq 0\right\}$ needs to be fulfilled. As the length scale of interest is typically well-above the physical scale of the diffuse transition between phases, we employ a multiphase-field model which explicitly decouples interfacial and bulk energy contributions [11, 26]. The free energy functional can thus be written as

$$\mathcal{F}(\boldsymbol{\phi}, \nabla\boldsymbol{\phi}, \boldsymbol{F}_{\text{el}}) = \int_{\Omega} \left\{f_{\text{interfacial}}(\boldsymbol{\phi}, \nabla\boldsymbol{\phi}) + f_{\text{bulk}}(\boldsymbol{\phi}, \boldsymbol{F}_{\text{el}})\right\} \, \mathrm{d}V,$$

where $\nabla\boldsymbol{\phi}$ denotes the tuple of respective gradients of $\boldsymbol{\phi}$. The interfacial contribution $f_{\text{interfacial}}$ is further composed of a gradient term $f_{\text{grad}}(\nabla\boldsymbol{\phi})$ and a potential term $f_{\text{pot}}(\boldsymbol{\phi})$ [52, 53]

$$f_{\text{interfacial}}(\boldsymbol{\phi}, \nabla\boldsymbol{\phi}) = -\varepsilon \sum_{\alpha} \sum_{\beta>\alpha} \gamma_{\alpha\beta} \nabla\phi_\alpha \cdot \nabla\phi_\beta + \frac{16}{\varepsilon\pi^2} \sum_{\alpha} \sum_{\beta>\alpha} \gamma_{\alpha\beta}\phi_\alpha\phi_\beta$$

which are formulated such that stable interface regions form between the grains with an interfacial energy of $\gamma_{\alpha\beta}$ in any $\alpha\beta$-interface [54]. Triple junction angles obey the sharp interface solution of Young's law [55]. The parameter ε scales the width of the diffuse interface in its normal direction [54] and is chosen in the following such that the diffuse transition is discretized by 8-10 grid points. The bulk free energy density term $f_{\text{bulk}}(\boldsymbol{\phi}, \boldsymbol{F}_{\text{el}})$ is formulated as the sum of phase-dependent contributions

$$f_{\text{bulk}}(\boldsymbol{\phi}, \boldsymbol{F}_{\text{el}}) = \sum_{\alpha=1}^{N} f_{\text{bulk}}^{\alpha} \phi_{\alpha},$$

where linear interpolation with the volume fraction ϕ_α is performed. Within this work, the bulk driving forces are purely elastic, i.e. $f_{\text{bulk}}^{\alpha} = f_{\text{el}}^{\alpha}(\boldsymbol{F}_{\text{el}}, k_i^{\alpha}, \boldsymbol{M}^{\alpha})$. The elastic free energy density f_{el}^{α} of phase α is calculated by means of eq. (7) inserting the phase-inherent quantities k_i^{α}, $i \in \{1, 2, 3, 4\}$ and $\boldsymbol{M}^{\alpha}$. The evolution of phase-field variables ϕ_α is governed by [8]

$$\dot{\phi}_\alpha = -\frac{1}{\tilde{N}\varepsilon} \sum_{\beta \neq \alpha}^{\tilde{N}} M_{\alpha\beta} \left(\frac{\delta f_{\text{interfacial}}}{\delta \phi_\alpha} - \frac{\delta f_{\text{interfacial}}}{\delta \phi_\beta} + \frac{8}{\pi} \sqrt{\phi_\alpha \phi_\beta} \left(\frac{\delta f_{\text{bulk}}}{\delta \phi_\alpha} - \frac{\delta f_{\text{bulk}}}{\delta \phi_\beta} \right) \right), \tag{12}$$

where $\tilde{N}(\boldsymbol{x}, t) \leq N$ denotes the number of phases which are locally present and $M_{\alpha\beta}$ is the pairwise mobility of an $\alpha\beta$-interface. Within this work, the evolution driven by energy minimization is used to create the initial morphology with well-defined diffuse interface regions. This is achieved by solving eq. (12) using a pseudo-time. Since the focus of this work is set on the impact of convective terms arising from mechanical deformation, phase transformation is not considered in the further course of the simulations for $t > 0$. In the absence of phase transformation, the phase variable of a material point $\boldsymbol{X}$ does not change in time, and thus the material time derivative vanishes leading to the set of purely convective transport equations

$$\forall \alpha = 1, \ldots, N: \qquad \dot{\phi}_\alpha = \frac{\partial \phi_\alpha}{\partial t} + \boldsymbol{v} \cdot \nabla \phi_\alpha = 0. \tag{13}$$

Consequently, the phase-variables are transported by the convective term of the material derivative, under a given velocity field arising from the mechanical deformation. For the discretisation of the convective term in eq. (13), different numerical schemes can be employed including standard schemes like upwind or central differences but also advanced flux-limiter schemes. The numerical solution introduces discretisation errors leading to undesired distortion and widening of the phase-fields interface even in absence of velocity gradients. The magnitude of those numerical errors depend on the resolution and the discretisation scheme [56]. In order to preserve stability, a certain amount of numerical diffusion is required, which comes along with lower order of accuracy though. In the past, several discretisation schemes have been constructed for such transport problems in order to maintain as much accuracy as possible while ensuring stability. Amongst those are schemes, that introduce a flux limiter in such a way, that the condition of a total variation diminishing (TVD) discretisation is fulfilled [57]. A commonly used TVD-scheme is the one of van Leer [58]. However, even the most sophisticated discretisation schemes introduce discretisation errors, that are accumulative in time leading to a deviation of the phase-field equilibrium profile as can be seen in Appendix A.

2.5. Phase-field mapping

Instead of directly solving the phase-field transport via eq. (13), we employ a novel mapping technique in order to avoid large errors arising from the discretisation (discussed in the previous paragraph). This *Phase-field mapping* uses the initial configuration such, that each phase-field $\phi_\alpha(\boldsymbol{x}, t)$ at any spatial position $\boldsymbol{x}$ and time t is set from the initial phase-field $\phi_\alpha^0(\boldsymbol{X})$ by the following parametrization,

$$\forall \alpha = 1, \ldots, N: \qquad \phi_\alpha(\boldsymbol{x}, t) = \phi_\alpha^0\left(\boldsymbol{\xi}(\boldsymbol{x}, t)\right) = \phi_\alpha^0(\boldsymbol{X}). \tag{14}$$

Thus $\phi_\alpha(\boldsymbol{x}, t)$ in the current configuration is retrieved by mapping the current position to the initial position and assigning the corresponding value of the initial phase-field, which is known from the initial conditions. Equation (14)

essentially implies, that the phase-field of a material point does not change in time. However, it would also be possible to consider phase-transformation in the initial configuration, such that $\partial \phi_\alpha^0 \left(\boldsymbol{X}, t \right) / \partial t \neq 0$, since the mapping only tracks the change in phase-field due to the deformation. In order to apply the mapping (14), the inverse motion field $\boldsymbol{\xi}$ needs to be known to retrieve the initial position $\boldsymbol{X}$ of any material point. In the current configuration, $\boldsymbol{\xi}$ is computed from the convective transport equation eq. (1). Note, that calculation of the inverse motion $\boldsymbol{\xi}$ is also required to solve for the deformation gradient and, therefore, does not add any additional computational cost for the phase-field update. With larger number N of phases, this feature gets even more considerable, since otherwise the equation system (13) with N equations needs to be solved, which is avoided by the mapping. A similar mapping approach has previously been used in the context of a level-set method by Cottet *et al.* [34] and in the sharp interface model of Dunne and Rannacher [59].

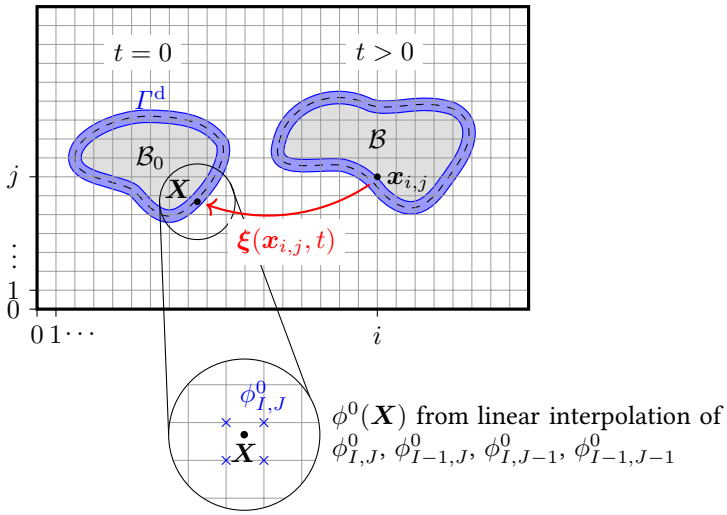

Figure 2: Diffuse interface representation of the body $\mathcal{B}$ in current and initial configuration on the numerical grid. Visualisation of the mapping approach and the interpolation of ϕ^0 in the initial configuration, where I, J correspond to the node indices in the initial configuration.

As the initial phase-field ϕ_α^0 is only saved at discrete grid points, an interpolation of the values ϕ_α^0 to the location $\boldsymbol{\xi}(\boldsymbol{x}, t)$ is done. The concept of the mapping and the interpolation in the initial configuration is illustrated in figure 2. In contrast to the numerical error of solving the transport equation, the interpolation error arising through this procedure is time independent and thus not accumulative. It is also possible, to save the initial phase-field with a higher grid resolution to further decrease the interpolation error without increasing computational cost. Since the inverse motion is also determined via a convective transport equation by means of eq. (1), the question of mapping accuracy arises. The main difference between the phase-field and the inverse motion are the initial conditions. While the phase-field exhibits locally steep gradients, as we deal with finite but small interfacial regions, the inverse motion is initially linear and thus the calculated gradient is exact. As evolution proceeds over time, the inverse motion function becomes less smooth if velocity gradients arise, which makes the numerical error problem dependent. For many cases, we expect gradients in $\boldsymbol{\xi}$ to be smaller than in ϕ, which leads to higher accuracy of equation (1) compared to (13). For the absence of velocity gradients, the inverse motion is always exactly obtained and the mapping approach preserves the shape almost perfectly, whereas the direct transport of the phase-field via eq. (13) in such a simple setup still accumulatively introduces large errors even for sophisticated schemes as shown in the example in Appendix A.

It has to be mentioned, that $\boldsymbol{\xi}$ may also point to a location outside the computational domain Ω, where $\boldsymbol{X} \notin \Omega$. An assumption for the phase-field ϕ_α^0 needs to be done in that case, which corresponds to the boundary conditions specifying the phase-field of inflowing matter, as they would also be required, if the transport equation (13) was employed. In this work, we use Neumann boundary conditions with zero normal gradient and thus ϕ_α^0 is set to the value of the nearest boundary node. E.g. if $\xi_x(\boldsymbol{x}, t) < 0$, then the value of $\phi_\alpha(\boldsymbol{x}, t) = \phi_\alpha^0([0, \xi_y, \xi_z]^\top, t)$ is assigned. It is straightforward to implement periodic or Dirichlet boundary conditions for the mapping approach.

3. Model validation

In the following subsections, the implementation of the large deformation framework with the cubic-anisotropic Kambouchev material model in Eulerian configuration is validated. First, simple load cases (i.e. simple shear, uniaxial tension and compression) are considered in Sec. 3.1. Next, the influence of the cubic anisotropy and its parameters on the material response of multiphase/polycrystalline systems under large deformations is systematically investigated in Sec. 3.2 and 3.3. The chosen material properties (i.e. Young's modulus E and Poisson ratio ν) along with the other derived material parameters are listed in table 1. Other system-specific parameters are specified in the respective sections.

Table 1: Material parameters used in the simulations

Parameters	Symbol	Expression	Value
Young's modulus	E	–	0.210
Poisson's ratio	ν	–	0.3
Lamé parameter 1	λ	$\frac{E\nu}{(1+\nu)(1-2\nu)}$	
Lamé parameter 2	μ	$\frac{E}{2(1+\nu)}$	

3.1. Isotropic material response under simple shear

As a starting point, we validate the model implementation by simulating the purely isotropic material response under simple shear and uniaxial loading. The analytical relations are derived and, thereafter, the numerically obtained material responses from the simulations are compared with these relations.

We consider a square specimen embedded in a matrix under the boundary conditions of simple shear as shown in figure 3a. The material properties (i.e. Young's modulus E and Poisson's ratio ν) of the specimen and matrix are chosen to be identical as given in table 1 which allows for visualization and validation of the diffuse interface approach in the Eulerian framework. The velocity is set to zero at vertical boundaries while the deformation is prescribed on the horizontal edges, either using Dirichlet (i.e. $u_1 = \bar{u}$) or Neumann (i.e. $t_1 = \bar{t}$) boundary conditions. The numerical setup with the diffuse interface description is depicted in Fig. 3b. For the case of simple shear, the deformation gradient $\boldsymbol{F}$ and the Right Cauchy-Green deformation tensor $\boldsymbol{C}$ are given by

$$\boldsymbol{F} = \begin{bmatrix} 1 & F_{12} & 0 \\ 0 & 1 & 0 \\ 0 & 0 & 1 \end{bmatrix} \quad \Longrightarrow \quad \boldsymbol{C} = \boldsymbol{F^T F} = \begin{bmatrix} 1 & F_{12} & 0 \\ F_{12} & 1+F_{12}^2 & 0 \\ 0 & 0 & 1 \end{bmatrix}.$$

Using the isotropic Kambouchev material law (eq. (10), with $k_3 = 0$), we obtain the following analytical equations for the non-zero stress components σ_{11}, σ_{12} and σ_{21}

$$\sigma_{11} = \mu F_{12}^2 \quad \text{and} \quad \sigma_{12} = \sigma_{21} = \mu F_{12} \tag{15}$$

of the Cauchy stress tensor $\boldsymbol{\sigma}$ in terms of the non-zero component F_{12} of the deformation gradient. For this deformation mode, simulations were performed under two different boundary conditions: 1) traction force or 2) displacement, as illustrated in Fig. 3a. We varied the values of the traction force component $t_1 = \bar{t}$ or displacement $u_1 = \bar{u}$, and the non-zero components of the Cauchy stress and deformation gradient are obtained at the mechanical equilibrium. The resulting stress-deformation response is plotted in Fig. 3c, along with the respective analytical relations (i.e. eq (15)). The numerically derived material response shows perfect match with the analytical equations. It is noteworthy that the modeling framework is capable of accurately simulating large shear deformations, with the shear deformation component F_{12} reaching a value upto 3.7, and as also visible in the inset pictures of the deformed specimen in Fig. 3c. A similar validation was performed for the case of uniaxial tension and, again, perfect agreement of simulations and analytics was found (see Section 1 of the Supplementary Material).

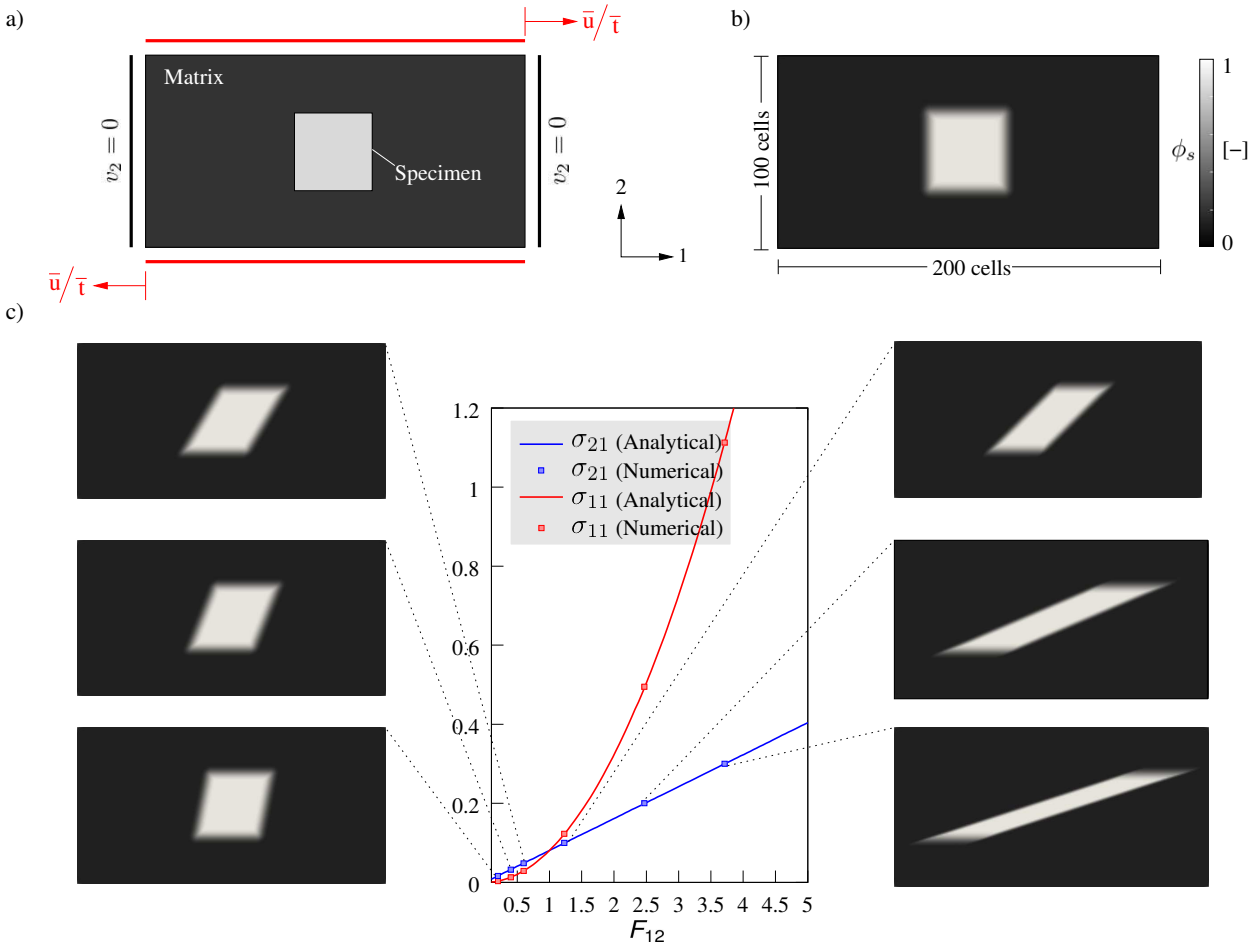

Figure 3: a) Boundary conditions of a 2-D square specimen embedded in a matrix of same material under simple shear load. b) Diffuse interface description of the problem where the phase-field $\phi_s \in [0, 1]$ determines the position of specimen in the computational domain. The plots of σ_{12}-F_{12} and σ_{11}-F_{12} under various boundary loads in the 1-direction on the surfaces normal to the 2-direction. The inset pictures depict the simulated deformation of the specimen under mechanical equilibrium.

3.2. Cubic-anisotropic material response

In this section, we validate the numerical implementation of cubic-anisotropy accounted by the non-zero anisotropic strength parameter k_3 in the material law eq. (10). We consider a rectangular inclusion embedded in a matrix of the same material as sketched in Fig. 4a. Both, matrix and inclusion, are chosen to exhibit cubic anisotropy described by the two orthogonal privileged directions, illustrated in the same figure. We denote the angle between the first privileged direction and the 1-direction by θ. On the vertical edges of this matrix-inclusion system, the Dirichlet boundary conditions (i.e. $u_1 = \pm\bar{u}$) corresponding to uniaxial compression are applied on the respective boundaries. For uniaxial loading, the deformation gradient $\boldsymbol{F}$ and Right Cauchy-Green tensor $\boldsymbol{C}$ are given analytically. The resulting stress from the Kambouchev law yields the non-zero components

$$\sigma_{11} = \left(\mu + \frac{\lambda}{2}\right)\left[F_{11} - \frac{1}{F_{11}}\right] + 4k_3 F_{11}\left[F_{11}^2 + 2\sin^2\theta\cos^2\theta\left(1 - F_{11}^2\right)\right], \tag{16a}$$

$$\sigma_{22} = \frac{\lambda}{2}\left[F_{11} - \frac{1}{F_{11}}\right] + \frac{4k_3}{F_{11}}\left[1 + 2\sin^2\theta\cos^2\theta\left(F_{11}^2 - 1\right)\right], \text{ and} \tag{16b}$$

$$\sigma_{12} = 4k_3\sin^2\theta\cos^2\theta\left(F_{11}^2 - 1\right)\left(\cos^2\theta - \sin^2\theta\right), \tag{16c}$$

which can be used for validation.

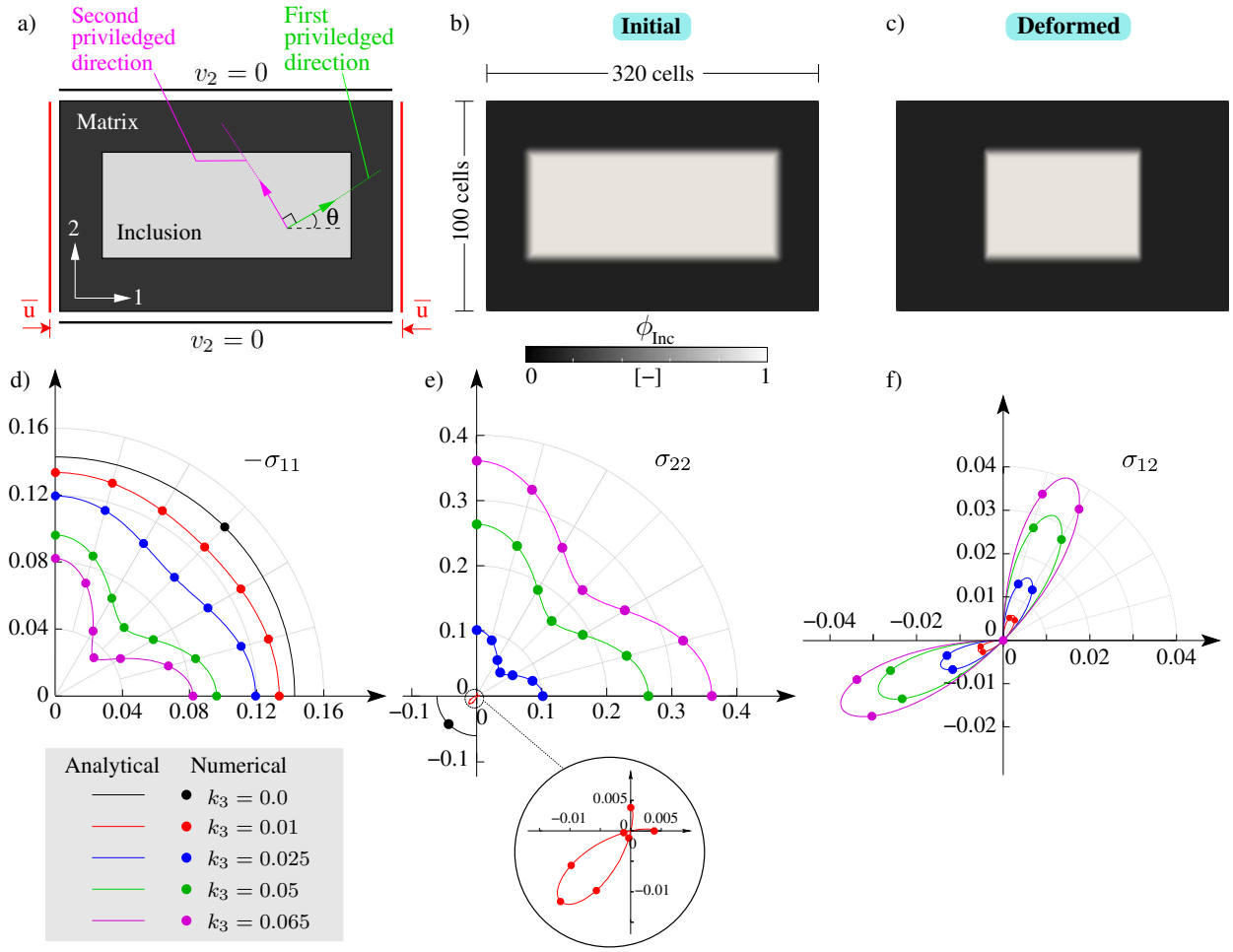

Figure 4: a) Boundary conditions of a 2-D rectangular inclusion embedded in a matrix of same material under uniaxial compressive load. The symbol θ denotes the angle of the first priviledged direction with respect to the 1-direction. b) Diffuse interface description of the problem where the phase-field $\phi_{\text{Inc}} \in [0, 1]$ determines the position of inclusion in the computational domain. c) Deformed configuration of the inclusion at the mechanical equilibrium for the case with $\theta = \pi/6$ and $k_3 = 0.065$. Polar plots of d) -σ_{11}, e) σ_{22} and f) σ_{12} as a function of θ. The numerical results match well with the analytical relations.

Figure 4b depicts the diffuse interface description of the system at the unloaded state. For different values of the anisotropic strength parameter k_3 and the angle θ, simulations were performed. Figure 4c shows the deformed state of the inclusion at mechanical equilibrium for $\theta = \pi/6$ and $k_3 = 0.065$, with a slight shear deformation due to the presence of non-zero shear stress σ_{12}, as also expected from eq. (16c). For this case, all the components of the Cauchy stress tensor $\boldsymbol{\sigma}$ are homogeneous in the complete domain, and their magnitudes are $\sigma_{11} = -0.0448$, $\sigma_{22} = 0.2629$ and $\sigma_{12} = -0.0349$. We plot the variation of $-\sigma_{11}$, σ_{22} and σ_{12} as a function of θ and anisotropic strength parameter k_3, both from the analytical relations of eq. (16) and those obtained from the simulations, see figures 4d-f. The numerically obtained variations of the stress components match well with the analytical relations, thereby validating the implementation of the Cubic-anisotropic Kambouchev material model in the present simulation framework. With the increasing value of anisotropic strength parameter k_3, the stress components are observed to become strongly dependent on the orientation θ, as expected. For the given boundary conditions, from the plots of the normal stress components σ_{11} and σ_{22} in figure 4d-e, as the value of k_3 increases, the $-\sigma_{11}$ component decreases while σ_{22} component increases. This essentially implies that phase with higher value of k_3 exhibits a lower compressive stiffness in 1-direction and higher tensile stiffness in the 2-direction.

3.3. Multi-phase system with varying anisotropy strength

Next, we study the impact of cubic anisotropy in multiphase/polycrystalline systems where each phase α may exhibit different anisotropic strength parameters k_3^α and may be oriented differently in space, where the crystallographic orientation is characterized by the phase-dependent angle θ^α of the first priviledged direction with respect to the 1-axis. Note, that in the diffuse interface, stresses are calculated using the linear interpolation

$$\boldsymbol{\sigma} = \sum_{\alpha=1}^{N} \phi_\alpha \boldsymbol{\sigma}_\alpha$$

of the phase inherent stresses $\boldsymbol{\sigma}_\alpha(\boldsymbol{F}, k_i^\alpha, \boldsymbol{M}^\alpha, \eta^\alpha, \zeta^\alpha)$. Herein, the elastic stress is obtained by means of eq. (9), where $\boldsymbol{M}^\alpha$ and k_i^α, $i \in \{1,2,3,4\}$ refer to the phase inherent structural tensor and elastic parameters of phase α, respectively. The viscous part is accounted for by eq. (11). The choice $\zeta^\alpha = \eta^\alpha = 0$ of the phase-inherent viscosities results in purely elastic behaviour, while non-zero values leads to visco-elastic material response. Instead of linear interpolation, more sophisticated diffuse interface approximations like the one proposed in Schneider *et al.* [31], which satisfies both the balance of linear momentum on a singular surface and the Hadamard condition, could also be adopted to the Eulerian framework. This is part of future work.

We consider a bar under uniaxial compression with the boundary displacement $\bar{u} = L/8$, where L corresponds to the domain length. Two cases are considered, where a different amount of phases are combined in series as depicted in figures 5a,b. For case 1 two phases are combined in series, whereas in case 2 four phases are considered. For all phases both cases, the orientation $\theta^\alpha = 0^o$ (where $\alpha \in \{\mathrm{A}, \mathrm{Matrix}\}$ in case 1 and $\alpha \in \{\mathrm{A}, \mathrm{B}, \mathrm{C}, \mathrm{Matrix}\}$ in case 2) of the first priviledged direction was set, while different values of the anisotropic strength parameters were chosen, given in the caption of the figure. The deformed states under mechanical equilibrium are depicted in figures 5c,d. We analyse the mechanical response for the two cases. For both cases, a homogeneous stress component σ_{11} is obtained in the whole domain with the values of -0.081 and -0.09 for the case 1 and 2, respectively. Moreover, as the orientation is $\theta = 0^o$, no shear stresses (i.e. $\sigma_{12} = 0$) occur in both cases. We analyse the non-zero fields (i.e the component F_{11} of the deformation gradient and the normal stress component σ_{22}). Figure 5e-h depict the contour plots and the variation of F_{11} and σ_{22} along the white dashed line highlighted in figure 5c,d. In the bulk regions of different phases, we observe that the phase with a higher value of k_3^α exhibits a lower value of the component F_{11} of the deformation gradient (and thereby a larger compressive deformation) and, secondly, a higher value of the normal stress component σ_{22}. These results are consistent with the plots of σ_{11} and σ_{22} in Fig. 4d) and e). In the interface region between any two phases, a smooth variation of the F_{11} and σ_{22} fields is observed, owing to the smoothly varying phase-fields of the respective phases.

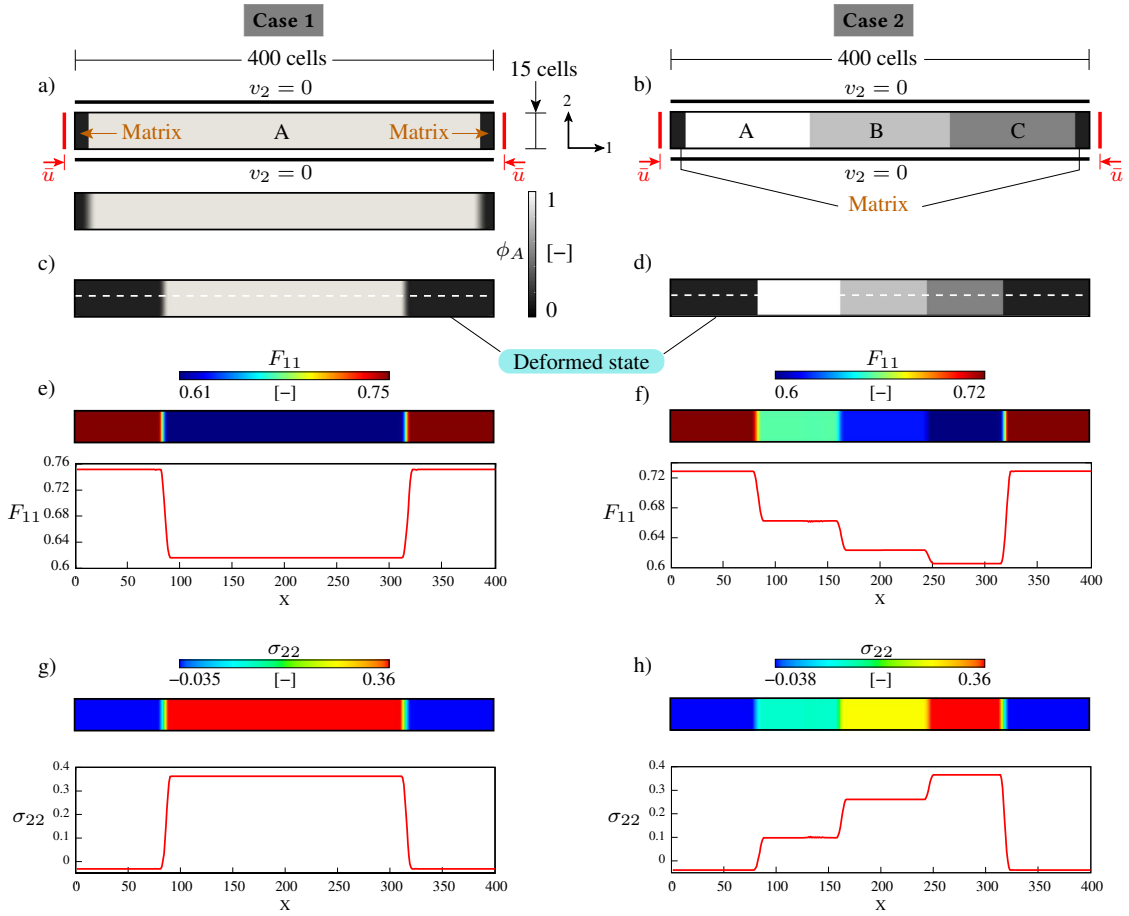

Figure 5: a) Numerical setup and boundary conditions of a 2-D two-phase bar with phases A and matrix, combined in series. The matrix is isotropic, while the phase A is anisotropic with the strength parameter $k_3^A = 0.065$. The diffuse interface description of the problem is given below. b) Deformed state of the bar. The contour plots along with the field variation along the white dashed lines (shown in part b) of the same figure) for c) F_{11} component of the deformation gradient and d) σ_{22} component of the Cauchy stress. e) Numerical setup and boundary conditions of the multiphase bar with four different phases namely A, B, C and matrix, combined in series. The matrix is isotropic, whereas the phases A, B and C are anisotropic with the phase-specific anisotropic strength parameters $k_3^A = 0.025$, $k_3^B = 0.05$ and $k_3^C = 0.065$. f) Deformed state of the bar. The contour plots along with the field variation along the white dashed line (shown in part a of the same figure) for g) F_{11} component of the deformation gradient and h) σ_{22} component of the Cauchy stress.

4. Application examples

4.1. Battery electrode calendering on the nano-scale

On the microscale, electrodes are composed of a network of particles, binder and pores with a porosity of about 50-60% after the drying process [60, 61]. The compaction during calendering is necessary to achieve higher energy densities and is carried out by applying mechanical pressure through rollers. This procedure results in an irreversible compaction through elimination of larger pore spaces which also includes breaking of previously existing binder connections as well as plastic deformation and fracture of active material particles. Modeling this process is rather difficult due to the multiple effects occurring simultaneously and the computational expense of moving interfaces, solid-body contact and large deformations involved. At sub-microscale, electrode particles often exhibit a polycrystalline structure, e.g. NMC and NCA cathodes for Li-ion batteries [62] as shown in Fig. 6a. These crystals may exhibit anisotropic material properties which need to be accounted for to provide an accurate description of the resulting stresses as well as the onset of fracture. We consider a simplified model system of polycrystalline material, analogous to a portion of an electrode particle, with four randomly oriented grain phases. At the left and right boundary, a matrix phase is introduced to apply the compaction pressure within the Eulerian framework. This

would not be necessary in the application with a fully-resolved electrode microstructure. The numerical setup and the boundary conditions of this system are shown in Fig. 6b.

The Young's modulus and Poisson's ratio of all the phases are chosen as given in Tab. 1. The phase-dependent anisotropic strength parameters are chosen to be identical, i.e. $k_3^A = k_3^B = k_3 = k_3^D = k_3^{\text{matrix}} = 0.01$. However, all the phases differ in the crystallographic orientation, with the angles of the first priviledged direction with respect to the 1-direction given by $\theta^{\text{A}} = 30^o$, $\theta^{\text{B}} = 15^o$, $\theta^{\text{C}} = 60^o$, $\theta^{\text{D}} = 45^o$ and $\theta^{\text{matrix}} = 0^o$, as schematically illustrated in figure 6b. The simulation was performed under a displacement-driven setting with $\bar{u} = 5L/60$, where L is the total domain length. Fig. 6c shows the deformed state of the system. The contour plots of different components of the displacement and stress are shown in figures 6d-h. Due to the differences in the crystallographic orientation of the phases, all the resulting fields are non-homogeneous in the computational domain. It is to be noted that, due to the diffuse nature of the interfaces in the system (characterized by the phase fields), these fields show a transition across the grain boundaries. This example illustrates the potential of the presented framework to also address mechanics on the nano-scale during the calendering process.

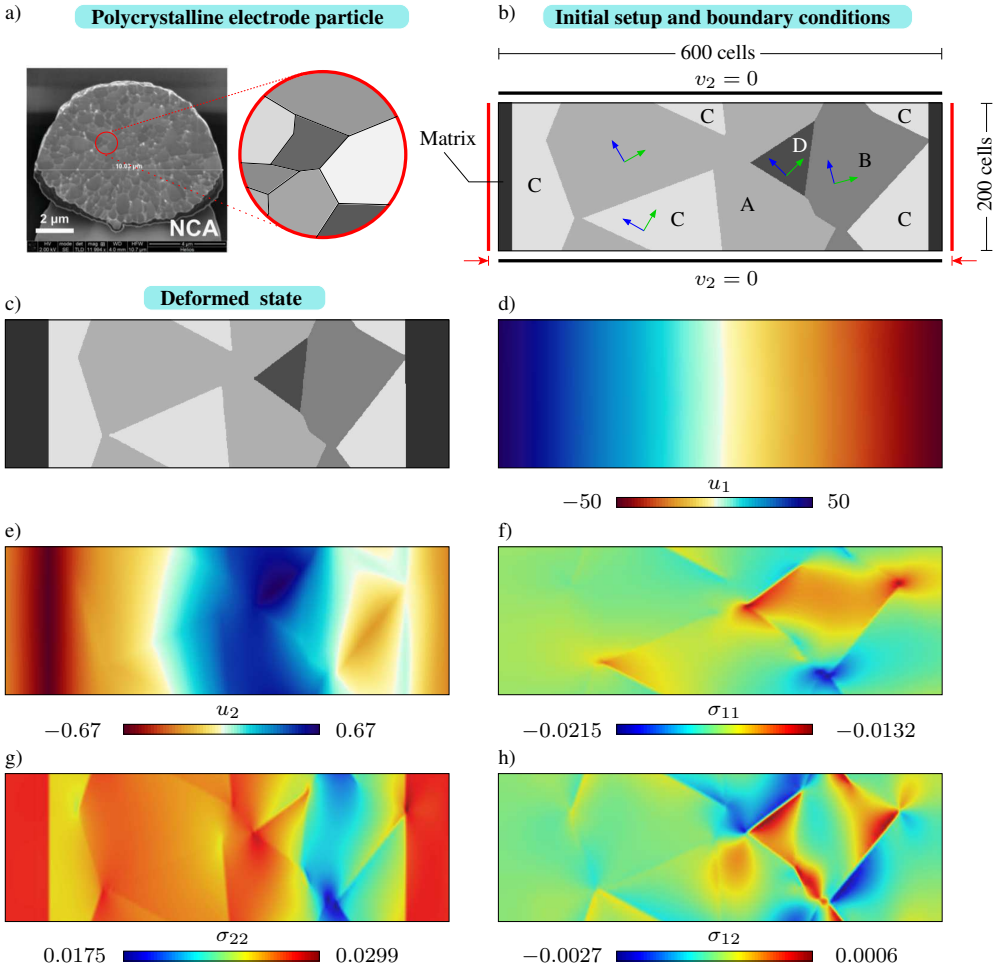

Figure 6: a) SEM of cross-section of a spherical NCA single particle exhibiting polycrystalline structure at submicroscale as schematically shown in the zoomed inset picture. Figure adapted from Tsai *et al.*(2018) [62]. b) Numerical setup and boundary conditions for a polycrystalline system laterally covered by a matrix. Different phases are shown in different shades of grey for the sake of visualization. c) The deformed state of the system. The contour plots of the displacement fields d) u_1 in the 1-direction and e) u_2 in the 2-direction. Contour plots of the resulting stress components f) σ_{11}, g) σ_{22} and h) σ_{12} in the computational domain. Due to the differences in the crystallographic orientation, the displacement and stress fields are non-homogeneous, and exhibit transition across the grain boundaries.

4.2. *Aerogel under compressive load*

The second example encompasses the compression of a two-layer composite consisting of two open-pore foams with different stiffnesses. These nano-structured and open-pore materials are called aerogels if the pore space is filled with air and can be made from various material classes such as silica, metals or organic materials [63]. Due to their low density combined with unique thermal and mechanical properties, they can be found in a huge range of applications, e.g. construction, life sciences and chemical engineering [63].

The initial setup shown in Fig. 7 a) includes two layeres of aerogel which can be periodically extended in the x- and y-direction in the spirit of a representative volume element. The randomized morphology is obtained from Voronoi tessellation and subsequent creation of ligaments in all multi-junctions using the algorithm introduced by August *et al.* [64]. Each layer has an initial height of $0.5H_0$. The materials are modelled using an isotropic visco-elastic material law as introduced in the previous sections with an elastic modulus of $E_{\text{foam1}} = E_{\text{ref}}$ in the upper (blue) layer and $E_{\text{foam2}} = 0.5E_{\text{ref}}$ in the lower (orange) layer. Note that all material properties as well as stresses are given in a non-dimensionalized manner throughout this section. The pore space is filled with air modelled as a visco-elastic phase with vanishing shear modulus and a relatively low compression modulus ($E_{\text{air}} = 0.01E_{\text{ref}}$). Viscosity is used in this case to stabilize the convergence of simulations as the high contrast of stiffnesses (3 orders of magnitude) results in a numerically stiff problem. The simulation setup further includes two stiff plates ($E_{\text{foam2}} = 10E_{\text{ref}}$) on the top and bottom side of the domain to apply compressive loading as shown in Fig. 7a). All boundary conditions in x- and y-direction are periodic while the top and bottom sides are subject to a time-dependent displacement BC ramping from zero displacement at $t = 0$ to 25% of the total computational domain in the final state, i.e. $u_x^{\text{bottom}} = -u_x^{\text{top}} = 0.25H_0$. As a result, the two-layer foam structure is compressed to 47% of its initial height H_0.

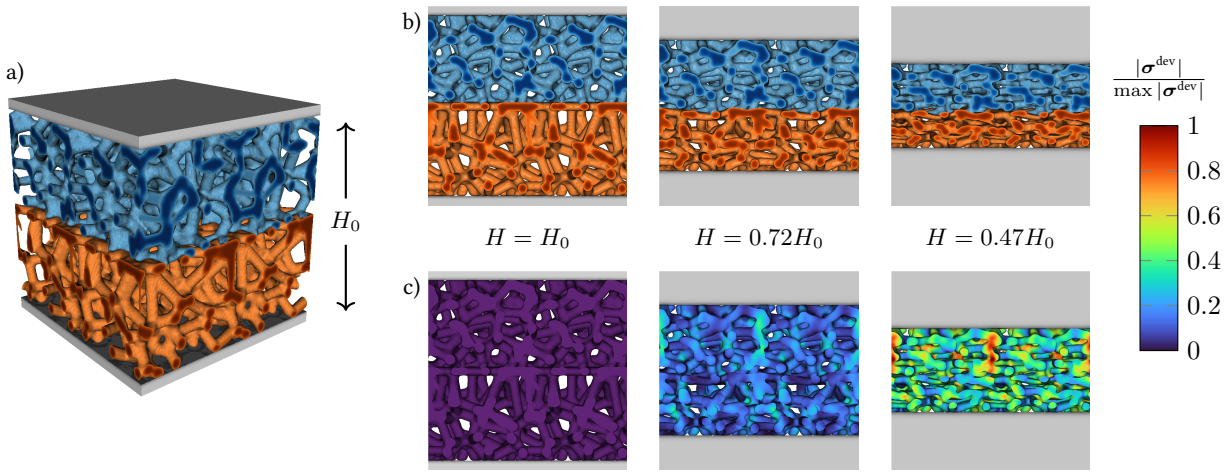

Figure 7: Compression of a two-layer foam structure with initial height H_0 in the three-dimensional setup shown in a). The upper layer (blue) exhibits twice the Young's modulus of the lower (orange) one. Different stages of deformation are shown in b) where the air phase is rendered transparent and the compressive plates are shown in gray. All phases are visualized by the iso-surfaces of $\phi_\alpha = 0.5$ which corresponds to the sharp interface problem. Subfigure c) shows the Frobenius-norm of the deviatoric part $\boldsymbol{\sigma}^{\text{dev}}$ of the Cauchy stress tensor normalized by its maximum value within the domain Ω.

The front view of the simulation domain in Fig. 7b) clearly shows a stronger compaction of the orange foam layer due to its lower stiffness. The corresponding stress state is visualized as the Frobenius-norm of the deviatoric part $\boldsymbol{\sigma}^{\text{dev}}$ of the Cauchy stress tensor, starting from a stress-free state in the initial configuration. Increasing the load leads to increasing stresses which are unevenly distributed in the complex network of ligaments. At even higher compression load, breaking or plastification of single ligaments as well as self-contact of the foam structure would be observed in experiments which pose severe computational challenges. Due to the small but non-zero stiffness of the air phase ($E_{\text{air}} = 0.01E_{\text{ref}}$), a thin layer remains between ligaments when they would get in contact. Treating the pore phase as a fluid with zero elastic stiffness rises the problem of correct interpolation within the diffuse interface regions. Once two solid bodies get in contact, the reference map of the contact point would be pointing to two different locations

in the reference configuration which can not be handled by the current definition of the deformation gradient in Eq. (2). A possible solution is the usage of individual $\boldsymbol{\xi}$-fields for each solid phase and a proper extrapolation of those fields into the pore phase as in the work of Valkov *et al.* [46]. This treatment allows for phase-inherent deformation gradients and thus stresses, which could be appropriately interpolated in the diffuse interface regions [30–32]. Such an approach within the Eulerian framework already captures the contact of solid bodies like the active particles without further need to pre-define surfaces that might come into contact at later simulation times as is the standard procedure in Lagrangian descriptions. Extension of the model in that direction will be subjected to future work. The application example highlights the model's ability to account for large deformations in complex, three-dimensional microstructures.

4.3. Deformation of a visco-elastic biological cell

The stiffness of biological cells is an indicator used for e.g. disease diagnosis. In order to measure it, real-time deformability cytometry can be used where cells are transported through a channel by fluid flow and their resulting deformation allows to determine the stiffness [2]. In this section, a simulation setup which replicates such experiments is used as an example of fluid structure interaction but the proposed framework is by no means limited to this special case. Since fluid flow is naturally described in the Eulerian framework, it is favourable to model both fluid and solid in the same configuration. Within the present model, the motion of a fluid can be treated by consideration of a visco-elastic phase with vanishing shear modulus and no anisotropy. From eq. (10) and (11), the stress relation

$$\boldsymbol{\sigma}^\alpha = \frac{\lambda^\alpha}{2}(J - J^{-1})\boldsymbol{I} + \eta^\alpha \left(\nabla \boldsymbol{v} + \nabla^\top \boldsymbol{v}\right) + \left(\zeta^\alpha - \frac{2}{3}\eta^\alpha\right) \nabla \cdot \boldsymbol{v}\, \boldsymbol{I}$$

can be derived which corresponds to a weakly compressible fluid cf., e.g., [65]. The assumption of weakly compressible fluids corresponds to neglecting the temperature-dependence of the pressure and thus, the equation of state is only density dependant yielding $p(\rho)$. Note, that $J^{-1} = \rho/\rho^0$ holds and λ^α acts as phase-inherent compressibility modulus in this case. Thus, we obtain the equation of state $p = \lambda(J^{-1} - J)/2$ which can be linearized around $J^{-1} = 1$ to yield the widely used relation $p = \lambda(J^{-1} - 1)$ [66]. Since J is obtained from the inverse motion, we do not need to employ the mass balance equation for the fluid as e.g. in [65]. Thus the present model can account for weakly compressible fluids if complemented with suitable boundary conditions.

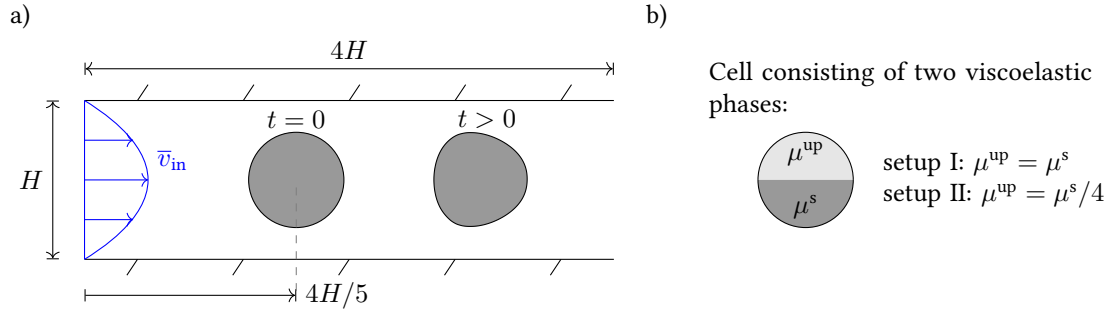

Figure 8: Viscoelastic sphere within a channel flow. a) problem setup including the initial shape at $t = 0$ and the final deformed shape plotted by means of the phase-field iso-surface with $\phi_{\text{f}} = 0.5$. b) Cell consisting of two phases: For setup I, the cell consists of one phase with μ^{s}, for setup II it consists of two phases with differing stiffness.

We consider the channel flow sketched in Fig. 8 subject to velocity boundary conditions using a parabolic inflow profile with mean velocity $\overline{v}_{\text{in}}$. The cell is initially spherical with a diameter of $3H/5$, where H is the channel height. The density is chosen constant as $\rho^{\text{f}} = \rho^{\text{s}} = \rho$, where the superscripts f and s refer to fluid and solid, respectively. Thus gravity has no impact. The relevant characteristic numbers are the Reynoldsnumber $Re = \rho\overline{v}_{\text{in}}H/\eta^{\text{f}} = 0.17$, as well as the ratio $\mu^{\text{s}}H/(\eta^{\text{f}}\overline{v}_{\text{in}}) = 46$ between the elastic and viscous contribution. The further material parameters read

$$\lambda^{\text{s}} = \lambda^{\text{f}} = 100\mu^{\text{s}}, \quad \zeta^{\text{f}} = \eta^{\text{f}}/10, \quad \eta^{\text{s}} = \eta^{\text{f}}/2, \quad \zeta^{\text{s}} = \eta^{\text{f}}/20.$$

In order to show the model's ability to also consider multiphase systems, we conduct a similar simulation, where the cell persists of two phases, which initially take the upper and lower half of the sphere, respectively. The phase in the upper part of the body has a reduced shear modulus of $\mu^{\text{up}} = \mu^{\text{s}}/4$, while all other parameters are kept unchanged.

Figure 9a shows the deformation of the cell over time. The behaviour observed shows qualitatively good agreement with the literature e.g. to the results of Mokbel *et al.* [50]. However, quantitative comparison is not possible, since they consider a pipeflow instead of a channel flow and employ incompressible modelling for both fluid and solid alongside a Neo-Hooke law for the latter. So far, we also neglect surface tension effects, which however can straightforwardly be added in context of the phasefield method by using a capillary stress tensor, which depends on $\nabla\phi$ (see e.g. [15]). Figure 9b shows the spatial distribution of the elastic stress part σ_{11}^{el} in the cell. Note, that within the cell, the velocity gradient becomes extremely small and thus the viscous stress is negligible there. Additionally, the final shapes for both the case with a single and two solid phases are depicted in figure 9c. In the latter case, the mismatch of shear moduli between upper and lower part of the cell introduces a clearly unsymmetrical behaviour. This is also observed in the simulation snapshots depicted in figure 10, where the F_{11} component of the deformation gradient is depicted. The values of F_{11} range from 0.2-1.7 in the fluid phase and from 0.9-1.05 in the cell. The Jacobi determinant J ranges from 0.98-1 with the chosen parameters.

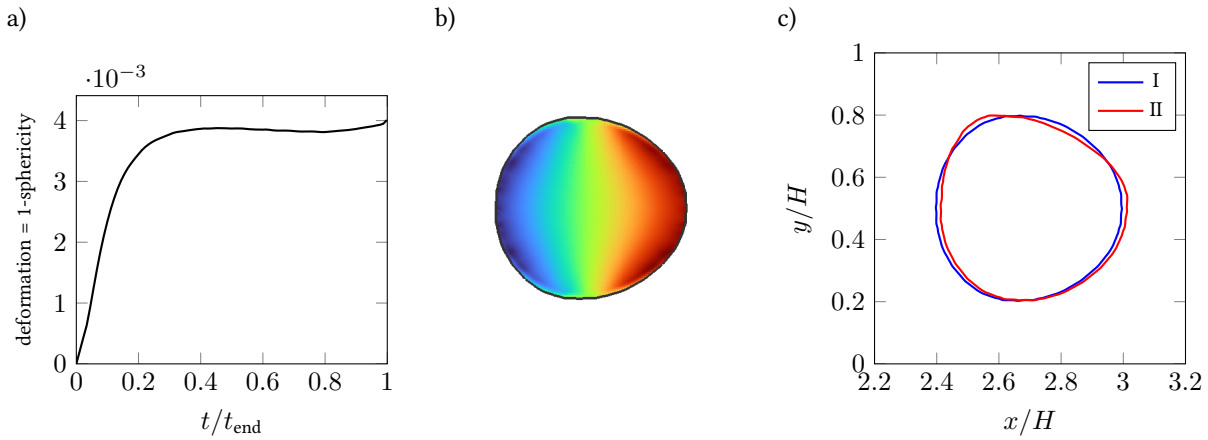

Figure 9: Deformation of the cell. a) cell deformation over time by means of $1 - S = 1 - 2\sqrt{A\pi}/P$, where S is the sphericity, A the area and P the perimeter of the 2D cell. b) Distribution of elastic stress σ_{11}^{el} in the cell. c) Cell shape at $t = t_{\text{end}}$ for the case, where the cell persists of one solid phase (I) and the case where it consists of two (II), with the upper part exhibiting a lower shear modulus.

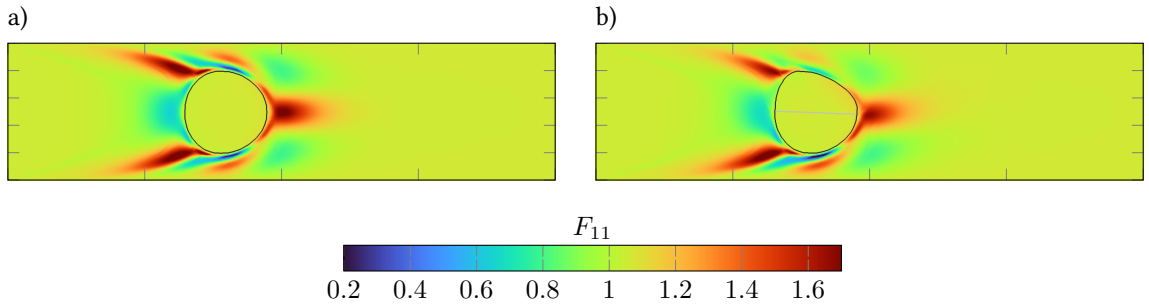

Figure 10: Snapshot of the simulation showing the F_{11}-component of the deformation gradient. The black line represents the 0.5 iso-contour of the fluid phase. a) Case I with single solid phase. b) Case II with two solid phases, where the gray line represents the solid-solid interface.

5. Conclusion and Outlook

In this article, we present a generalized and rigorous computational framework for simulating large deformation processes in multiphase and polycrystalline materials based on a phase-field approach. The framework is well-suited for a variety of applications like modelling the calendering process for battery electrode manufacturing, deformation of foam structures like aerogels as well as fluid-structure interaction. The model is validated on benchmark examples and possible model extensions are discussed and sketched in this work e.g. the consideration of non-solid pore phases. We chose a formulation in the Eulerian configuration for several reasons. Firstly, with this model, mesh distortions and the associated numerical issues of the Lagrangian approaches are obviated, which allows for consideration of very large deformations as shown in Fig. 3. Secondly, the Eulerian framework offers the potential to treat contact of different solid bodies naturally without the need for interface tracking. Additionally, extensions in several directions that are well-suited for addressing coupled multiphysics are possible. The primary contributions and highlights of this work are summarized in the following points:

1. A key novel feature of the computational model is the developed *phase-field mapping method* for tracking the location of interfaces (i.e. grain boundaries) of a multiphase system undergoing large mechanical deformation. With this method, the numerical errors generated by the discretisation of the convective terms (in the balance relation) using traditional convection schemes are avoided because this method retrieves the position of the interface by utilizing the evolution equation for the reference map. Superiority of phase-field mapping in comparison with other convection schemes is clearly visible in applications with large displacement like the rigid body motion demonstrated in Appendix A.
2. The poly-convex material model with cubic anisotropy [45] is employed as the constitutive relationship. We formulate this with respect to the Cauchy stresses in order to incorporate it within the Eulerian framework. Unlike the conventional Saint Venant Kirchoff law, this material model is polyconvex in nature, ensuring the occurrence of a energetic minimum. Analytical relations for simple cases were derived for this material model, and the numerical implementation has been validated using numerical benchmark problems. Additionally, the consideration of Kelvin-Voigt viscoelastic behaviour can naturally be included in the proposed framework. The simulation results proof that the current model is capable of simulating extremely large deformations. Within the multi-phase field framework, each phase can exhibit distinct material behaviour by assigning different material properties to it, such as varying stiffness, cubic anisotropy as well as zero or non-zero viscosity.
3. We demonstrate applicability in the context of the calendering process for battery electrode manufacturing at the nano-scale. Owing to the incorporated anisotropy, the model can be employed to polycrystalline agglomerates where each primary particle features a different crystallographic orientation.
4. The compression of a two-layer aerogel highlights the model's ability to account for large deformations in complex, three-dimensional microstructures. The inclusion of viscous stresses ensures numerical convergence although the ratio of Young's moduli spans three orders of magnitude. Model limitations considering a pore phase with zero stiffness are discussed in detail.
5. The ability of the viscoelastic model to account for fluid structure interaction with weakly compressible fluids is shown exemplarily for biological cell in a channel flow.

Irreversible deformations can be included via the multiplicative split of the deformation gradient (eq. (3)), which allows for an extension towards temperature- or concentration-dependent inelastic strains as well as plasticity. The potential of model extension with the inclusion of general eigenstrains is discussed in more detail in Section 3 of the Supplementary Material. Furthermore, coupling large elastic deformations with other fields such as phase transformations and chemical driving forces is possible through the multiphase-field method.

Acknowledgments

This work contributes to the research performed at CELEST (Center for Electrochemical Energy Storage Ulm-Karlsruhe) and was funded by the German Research Foundation (DFG) under Project ID 390874152 (POLiS Cluster of Excellence). This work also contributes to the research performed under the financial support of by the Bundesministerium für Bildung und Forschung (BMBF) within the KMU-innovative project BioSorb as well as to the programme MSE no. 43.31.02 of the Helmholtz association.

Appendix A. Phase-field mapping vs other convection schemes: Rigid body motion

To demonstrate the problem of accumulative discretization errors during convective transport, we consider the motion of a star-shaped body parametrized with a phase-field as shown in figure A.11a. The body is transported within a constant velocity field $\boldsymbol{v} = v\boldsymbol{e}_x$. The convective transport equation (13) is solved employing different schemes for the discretisation of the convective term and compared with a simulation using the phase-field mapping method. Figure A.11b depicts the simulated rigid body motion at two different representative timesteps using different approaches. In particular, the performance of three convection schemes namely upwind scheme as well as total variation diminishing schemes with van Leer [58] and superbee [67] flux limiter are analysed in comparison to the phase-field mapping. It is observed, that the upwind scheme introduces enormous numerical diffusion, which leads to a complete loss of shape. The more advanced flux limiter schemes are able to better preserve the shape. The phase-field mapping method clearly stands out among these schemes, with no interface and shape distortion as depicted in the last row of figure A.11b. The reason for this is, that the inverse motion is exactly obtained by equation (1) due to the absence of velocity gradients. If velocity gradients occur, the mapping also leads to inaccuracies due to the numerical solution of the inverse motion function. However, these errors tend to be smaller than those from the direct convective transport of the phase-field as the velocity field often exhibits smaller local gradients.

References

[1] K. E. Kasza, A. C. Rowat, J. Liu, T. E. Angelini, C. P. Brangwynne, G. H. Koenderink, D. A. Weitz, The cell as a material, Current opinion in cell biology 19 (1) (2007) 101–107. doi:10.1016/j.ceb.2006.12.002.

[2] M. Mokbel, D. Mokbel, A. Mietke, N. Traber, S. Girardo, O. Otto, J. Guck, S. Aland, Numerical simulation of real-time deformability cytometry to extract cell mechanical properties, ACS Biomaterials Science & Engineering 3 (11) (2017) 2962–2973. doi:10.1021/acsbiomaterials.6b00558.

[3] A. E. Ekpenyong, G. Whyte, K. Chalut, S. Pagliara, F. Lautenschläger, C. Fiddler, S. Paschke, U. F. Keyser, E. R. Chilvers, J. Guck, Viscoelastic properties of differentiating blood cells are fate-and function-dependent, PloS one 7 (9) (2012) e45237. doi:10.1371/journal.pone.0045237.

[4] J. Lu, S. C. Chung, S.-i. Nishimura, A. Yamada, Phase Diagram of Olivine Na x FePO 4 (0 ¡ x ¡ 1), Chemistry of Materials 25 (22) (2013) 4557–4565. doi:10.1021/cm402617b.
URL https://pubs.acs.org/doi/10.1021/cm402617b

[5] S. Chung, A. Manthiram, Current Status and Future Prospects of Metal–Sulfur Batteries, Advanced Materials 1901125 (2019) 1901125. doi:10.1002/adma.201901125.
URL https://onlinelibrary.wiley.com/doi/abs/10.1002/adma.201901125

[6] L. Chen, F. Fan, L. Hong, J. Chen, Y. Z. Ji, S. L. Zhang, T. Zhu, L.-Q. Chen, A Phase-Field Model Coupled with Large Elasto-Plastic Deformation: Application to Lithiated Silicon Electrodes, Journal of The Electrochemical Society 161 (11) (2014) F3164–F3172. doi:10.1149/2.0171411jes.

[7] D. A. Cogswell, M. Z. Bazant, Theory of Coherent Nucleation in Phase-Separating Nanoparticles, Nano Letters 13 (7) (2013) 3036–3041. doi:10.1021/nl400497t.
URL https://pubs.acs.org/doi/10.1021/nl400497t

[8] I. Steinbach, Phase-field models in materials science, Modelling and Simulation in Materials Science and Engineering 17 (7) (2009). doi:10.1088/0965-0393/17/7/073001.

[9] N. Moelans, B. Blanpain, P. Wollants, An introduction to phase-field modeling of microstructure evolution, Calphad: Computer Coupling of Phase Diagrams and Thermochemistry 32 (2) (2008) 268–294. doi:10.1016/j.calphad.2007.11.003.

[10] J. Hötzer, A. Reiter, H. Hierl, P. Steinmetz, M. Selzer, B. Nestler, The parallel multi-physics phase-field framework PACE3D, Journal of Computational Science 26 (2018) 1–12. doi:10.1016/j.jocs.2018.02.011.
URL https://doi.org/10.1016/j.jocs.2018.02.011

[11] B. Nestler, H. Garcke, B. Stinner, Multicomponent alloy solidification: phase-field modeling and simulations, Physical Review E 71 (4) (2005) 041609.

[12] N. Prajapati, M. Selzer, B. Nestler, B. Busch, C. Hilgers, Modeling fracture cementation processes in calcite limestone: a phase-field study, Geothermal Energy 6 (1) (2018) 1–15.

[13] N. Prajapati, A. Abad Gonzalez, M. Selzer, B. Nestler, B. Busch, C. Hilgers, Quartz cementation in polycrystalline sandstone: Insights from phase-field simulations, Journal of Geophysical Research: Solid Earth 125 (2) (2020) e2019JB019137.

[14] N. Prajapati, M. Spaeth, L. Knecht, M. Selzer, B. Nestler, Quantitative phase-field modeling of faceted crystal dissolution processes, Crystal Growth and Design 21 (6) (2021) 3266–3279.

[15] D. Jacqmin, Calculation of two-phase navier–stokes flows using phase-field modeling, Journal of Computational Physics 155 (1) (1999) 96–127. doi:10.1006/jcph.1999.6332.

[16] H. Abels, H. Garcke, G. Grün, Thermodynamically consistent, frame indifferent diffuse interface models for incompressible two-phase flows with different densities, Mathematical Models and Methods in Applied Sciences 22 (03) (2012) 1150013. doi:10.1142/S0218202511500138.

[17] B. C. Han, A. Van Der Ven, D. Morgan, G. Ceder, Electrochemical modeling of intercalation processes with phase field models, Electrochimica Acta 49 (26) (2004) 4691–4699. doi:10.1016/j.electacta.2004.05.024.

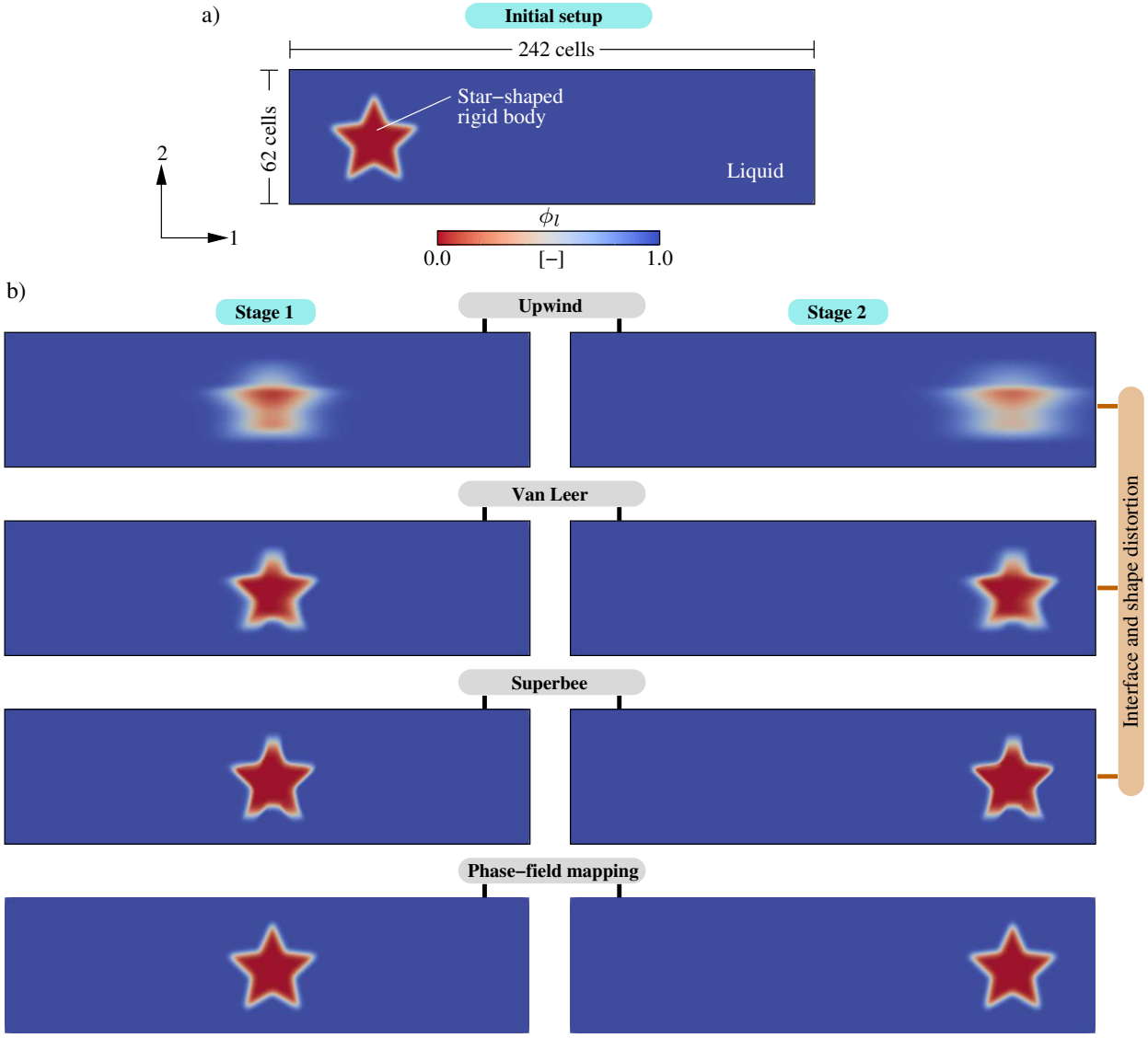

Figure A.11: a) Numerical setup for a star-shaped rigid body transported within a constant horizontal velocity field. Two timesteps of the simulated rigid body motion are shown comparatively for different convective schemes. The phase-field mapping shows superior performance in cases with weak velocity gradients while all other schemes exhibit substantial interface- and shape-distortion.

[18] S. Daubner, P. K. Amos, E. Schoof, J. Santoki, D. Schneider, B. Nestler, Multiphase-field modeling of spinodal decomposition during intercalation in an allen-cahn framework, Physical Review Materials 5 (3) (2021) 035406.

[19] L. Schöller, D. Schneider, C. Herrmann, A. Prahs, B. Nestler, Phase-field modeling of crack propagation in heterogeneous materials with multiple crack order parameters, Computer Methods in Applied Mechanics and Engineering 395 (2022) 114965.

[20] T. Q. Bui, X. Hu, A review of phase-field models, fundamentals and their applications to composite laminates, Engineering Fracture Mechanics 248 (2021) 107705. doi:10.1016/j.engfracmech.2021.107705.

[21] M. Ambati, T. Gerasimov, L. De Lorenzis, A review on phase-field models of brittle fracture and a new fast hybrid formulation, Computational Mechanics 55 (2) (2015) 383–405. doi:10.1007/s00466-014-1109-y.

[22] P. Zhang, X. Hu, S. Yang, W. Yao, Modelling progressive failure in multi-phase materials using a phase field method, Engineering Fracture Mechanics 209 (2019) 105–124. doi:10.1016/j.engfracmech.2019.01.021.

[23] Y. Wang, A. Khachaturyan, Three-dimensional field model and computer modeling of martensitic transformations, Acta Materialia 45 (2) (1997) 759–773. doi:10.1016/S1359-6454(96)00180-2.

[24] V. I. Levitas, Thermodynamically consistent phase field approach to phase transformations with interface stresses, Acta Materialia 61 (12) (2013) 4305–4319. doi:10.1016/j.actamat.2013.03.034.

[25] L.-Q. Chen, W. Yang, Computer simulation of the domain dynamics of a quenched system with a large number of nonconserved order parameters: The grain-growth kinetics, Physical Review B 50 (21) (1994) 15752–15756. doi:10.1103/PhysRevB.50.15752.
[26] I. Steinbach, F. Pezzolla, B. Nestler, M. Seeßelberg, R. Prieler, G. Schmitz, J. Rezende, A phase field concept for multiphase systems, Physica D: Nonlinear Phenomena 94 (3) (1996) 135–147. doi:10.1016/0167-2789(95)00298-7.
[27] E. Schoof, D. Schneider, N. Streichhan, T. Mittnacht, M. Selzer, B. Nestler, Multiphase-field modeling of martensitic phase transformation in a dual-phase microstructure, International Journal of Solids and Structures 134 (2018) 181–194. doi:10.1016/j.ijsolstr.2017.10.032.
[28] K. Ammar, B. Appolaire, G. Cailletaud, S. Forest, Combining phase field approach and homogenization methods for modelling phase transformation in elastoplastic media, European Journal of Computational Mechanics 18 (5-6) (2009) 485–523. doi:10.3166/ejcm.18.485-523.
[29] D. Schneider, O. Tschukin, A. Choudhury, M. Selzer, T. Böhlke, B. Nestler, Phase-field elasticity model based on mechanical jump conditions, Computational Mechanics 55 (5) (2015) 887–901. doi:10.1007/s00466-015-1141-6.
[30] J. Mosler, O. Shchyglo, H. Montazer Hojjat, A novel homogenization method for phase field approaches based on partial rank-one relaxation, Journal of the Mechanics and Physics of Solids 68 (1) (2014) 251–266. doi:10.1016/j.jmps.2014.04.002.
[31] D. Schneider, F. Schwab, E. Schoof, A. Reiter, C. Herrmann, M. Selzer, T. Böhlke, B. Nestler, On the stress calculation within phase-field approaches: a model for finite deformations, Computational Mechanics 60 (2) (2017) 203–217. doi:10.1007/s00466-017-1401-8.
[32] B. Svendsen, P. Shanthraj, D. Raabe, Finite-deformation phase-field chemomechanics for multiphase, multicomponent solids, Journal of the Mechanics and Physics of Solids 112 (2018) 619–636. doi:10.1016/j.jmps.2017.10.005.
[33] M. Kojic, Stress integration procedures for inelastic material models within the finite element method, Appl. Mech. Rev. 55 (4) (2002) 389–414.
[34] G.-H. Cottet, E. Maitre, T. Milcent, An eulerian method for fluid-structure coupling with biophysical applications, in: Proceedings of the European Conference on Computational Fluid Dynamics (ECCOMAS CFD 2006), 2006, pp. 1–16.
[35] S. Okazawa, K. Kashiyama, Y. Kaneko, Eulerian formulation using stabilized finite element method for large deformation solid dynamics, International Journal for Numerical Methods in Engineering 72 (13) (2007) 1544–1559. doi:10.1002/nme.2057.
URL http://doi.wiley.com/10.1002/nme.2057
[36] K. Kamrin, C. H. Rycroft, J.-C. Nave, Reference map technique for finite-strain elasticity and fluid–solid interaction, Journal of the Mechanics and Physics of Solids 60 (11) (2012) 1952–1969. doi:10.1016/j.jmps.2012.06.003.
[37] J. Hötzer, A. Reiter, H. Hierl, P. Steinmetz, M. Selzer, B. Nestler, The parallel multi-physics phase-field framework pace3d, Journal of computational science 26 (2018) 1–12. doi:10.1016/j.jocs.2018.02.011.
[38] E. Borukhovich, P. S. Engels, T. Böhlke, O. Shchyglo, I. Steinbach, Large strain elasto-plasticity for diffuse interface models, Modelling and Simulation in Materials Science and Engineering 22 (3) (2014). doi:10.1088/0965-0393/22/3/034008.
[39] Y. Sun, C. Beckermann, Sharp interface tracking using the phase-field equation, Journal of Computational Physics 220 (2) (2007) 626–653. doi:10.1016/j.jcp.2006.05.025.
[40] R. Hill, Constitutive Inequalities for Isotropic Elastic Solids Under Finite Strain, Proceedings of the Royal Society A: Mathematical, Physical and Engineering Sciences 314 (1519) (1970) 457–472. doi:10.1098/rspa.1970.0018.
[41] J. M. Ball, Convexity conditions and existence theorems in nonlinear elasticity, Archive for Rational Mechanics and Analysis 63 (4) (1976) 337–403. doi:10.1007/BF00279992.
URL http://link.springer.com/10.1007/BF00279992
[42] A. Raoult, Non-polyconvexity of the stored energy function of a Saint Venant-Kirchhoff material, Aplikace matematiky 31 (6) (1986) 417–419.
URL http://eudml.org/doc/15466
[43] C. Di Leo, E. Rejovitzky, L. Anand, A Cahn-Hilliard-type phase-field theory for species diffusion coupled with large elastic deformations: Application to phase-separating Li-ion electrode materials, Journal of the Mechanics and Physics of Solids 70 (1) (2014) 1–29. doi:10.1016/j.jmps.2014.05.001.
URL http://dx.doi.org/10.1016/j.jmps.2014.05.001
[44] T. Zhang, M. Kamlah, Sodium Ion Batteries Particles: Phase-Field Modeling with Coupling of Cahn-Hilliard Equation and Finite Deformation Elasticity, Journal of The Electrochemical Society 165 (10) (2018) A1997–A2007. doi:10.1149/2.0141810jes.
URL http://jes.ecsdl.org/lookup/doi/10.1149/2.0141810jes
[45] N. Kambouchev, J. Fernandez, R. Radovitzky, A polyconvex model for materials with cubic symmetry, Modelling and Simulation in Materials Science and Engineering 15 (5) (2007) 451. doi:10.1088/0965-0393/15/5/006.
[46] B. Valkov, C. H. Rycroft, K. Kamrin, Eulerian method for multiphase interactions of soft solid bodies in fluids, Journal of Applied Mechanics 82 (4) (2015) 041011. doi:10.1115/1.4029765.
[47] B. J. Plohr, D. H. Sharp, A conservative eulerian formulation of the equations for elastic flow, Advances in Applied Mathematics 9 (4) (1988) 481–499. doi:10.1016/0196-8858(88)90025-5.
[48] J. A. Trangenstein, P. Colella, A Higher-Order Godunov Approach for Modeling Finite Deformation in Elastic-Plasic Solids, Communications on Pure and Applied Mathematics 44 (1) (1991) 41–100.
[49] C. Liu, N. Walkington, An eulerian description of fluids containing visco-elastic particles, Archive for rational mechanics and analysis 159 (3) (2001) 229–252. doi:10.1007/s002050100158.
[50] D. Mokbel, H. Abels, S. Aland, A phase-field model for fluid–structure interaction, Journal of Computational Physics 372 (2018) 823–840. doi:10.1016/j.jcp.2018.06.063.
[51] J.-P. Boehler, Applications of tensor functions in solid mechanics, Vol. 292, Springer, Wien, 1987. doi:10.1007/978-3-7091-2810-7.
[52] I. Steinbach, F. Pezzolla, A generalized field method for multiphase transformations using interface fields, Physica D: Nonlinear Phenomena 134 (4) (1999) 385–393. doi:10.1016/S0167-2789(99)00129-3.
URL https://linkinghub.elsevier.com/retrieve/pii/S0167278999001293
[53] S. Daubner, M. Weichel, D. Schneider, B. Nestler, Modeling intercalation in cathode materials with phase-field methods: Assumptions and implications using the example of LiFePO4, Electrochimica Acta 421 (November 2021) (2022) 140516. doi:10.1016/j.electacta.

2022.140516.
[54] B. Nestler, H. Garcke, B. Stinner, Multicomponent alloy solidification: phase-field modeling and simulations, Physical Review E 71 (4) (2005) 41609.
[55] J. Eiken, Discussion of the Accuracy of the Multi-Phase-Field Approach to Simulate Grain Growth with Anisotropic Grain Boundary Properties, ISIJ International 60 (8) (2020) 1832–1834. doi:10.2355/isijinternational.ISIJINT-2019-722.
[56] F. Kemm, A comparative study of tvd-limiters – well-known limiters and an introduction of new ones, International Journal for Numerical Methods in Fluids 67 (4) (2011) 404–440. doi:10.1002/fld.2357.
[57] P. K. Sweby, High resolution schemes using flux limiters for hyperbolic conservation laws, SIAM journal on numerical analysis 21 (5) (1984) 995–1011. doi:10.1137/0721062.
[58] B. Van Leer, Towards the ultimate conservative difference scheme. ii. monotonicity and conservation combined in a second-order scheme, Journal of computational physics 14 (4) (1974) 361–370. doi:10.1016/0021-9991(74)90019-9.
[59] T. Dunne, R. Rannacher, Adaptive finite element approximation of fluid-structure interaction based on an eulerian variational formulation, in: Fluid-structure interaction, Springer, 2006, pp. 110–145.
[60] D. Schmidt, M. Kamlah, V. Knoblauch, Highly densified ncm-cathodes for high energy li-ion batteries: Microstructural evolution during densification and its influence on the performance of the electrodes, Journal of Energy Storage 17 (2018) 213–223.
[61] M. Müller, L. Schneider, N. Bohn, J. R. Binder, W. Bauer, Effect of Nanostructured and Open-Porous Particle Morphology on Electrode Processing and Electrochemical Performance of Li-Ion Batteries, ACS Applied Energy Materials 4 (2) (2021) 1993–2003. doi:10.1021/acsaem.0c03187.
URL https://pubs.acs.org/doi/10.1021/acsaem.0c03187
[62] P.-C. Tsai, B. Wen, M. Wolfman, M.-J. Choe, M. S. Pan, L. Su, K. Thornton, J. Cabana, Y.-M. Chiang, Single-particle measurements of electrochemical kinetics in nmc and nca cathodes for li-ion batteries, Energy & Environmental Science 11 (4) (2018) 860–871.
[63] J. Stergar, U. Maver, Review of aerogel-based materials in biomedical applications, Journal of Sol-Gel Science and Technology 77 (3) (2016) 738–752. doi:10.1007/s10971-016-3968-5.
[64] A. August, J. Ettrich, M. Rölle, S. Schmid, M. Berghoff, M. Selzer, B. Nestler, Prediction of heat conduction in open-cell foams via the diffuse interface representation of the phase-field method, International Journal of Heat and Mass Transfer 84 (2015) 800–808. doi:10.1016/j.ijheatmasstransfer.2015.01.052.
[65] C. C. S. Song, M. Yuan, A Weakly Compressible Flow Model and Rapid Convergence Methods, Journal of Fluids Engineering 110 (4) (1988) 441–445. doi:10.1115/1.3243575.
[66] K. D. Housiadas, G. C. Georgiou, New analytical solutions for weakly compressible newtonian poiseuille flows with pressure-dependent viscosity, International Journal of Engineering Science 107 (2016) 13–27. doi:10.1016/j.ijengsci.2016.07.001.
[67] P. L. Roe, Characteristic-based schemes for the euler equations, Annual Review of Fluid Mechanics 18 (1) (1986) 337–365. doi:10.1146/annurev.fl.18.010186.002005.